Effects of dark matter substructures on gravitational lensing: results from the Aquarius simulations

D. D. Xu,[1][*] Shude Mao,[1] Jie Wang,[2,3] V. Springel,[2] Liang Gao,[3,4] S. D. M. White,[2] Carlos S. Frenk,[3] Adrian Jenkins,[3] Guoliang Li[5] and Julio F. Navarro[6]

[1]*Jodrell Bank Centre for Astrophysics, University of Manchester, Alan Turing Building, Manchester M13 9PL*
[2]*Max-Planck Institut Für Astrophysik, Karl-Schwarzschild-Straße 1, 85740 Garching, Germany*
[3]*Institute of Computational Cosmology, Department of Physics, University of Durham, South Road, Durham DH1 3LE*
[4]*National Astronomical Observatories, Chinese Academy of Sciences, Beijing, 100012 China*
[5]*Argelander-Institut für Astronomie, University of Bonn, Auf dem Hügel 71, D-53121 Bonn, Germany*
[6]*Department of Physics and Astronomy, University of Victoria, Victoria, BC, V8P, 5C2 Canada*

ABSTRACT

We use the high-resolution Aquarius simulations of the formation of Milky Way-sized haloes in the Λ cold dark matter cosmology to study the effects of dark matter substructures on gravitational lensing. Each halo is resolved with $\sim 10^8$ particles (at a mass resolution $m_p \sim 10^3$ to $10^4 \, h^{-1} \, \mathrm{M_\odot}$) within its virial radius. Subhaloes with masses $m_{sub} \gtrsim 10^5 \, h^{-1} \, \mathrm{M_\odot}$ are well resolved, an improvement of at least two orders of magnitude over previous lensing studies. We incorporate a baryonic component modelled as a Hernquist profile and account for the response of the dark matter via adiabatic contraction. We focus on the 'anomalous' flux ratio problem, in particular on the violation of the cusp–caustic relation due to substructures. We find that subhaloes with masses less than $\sim 10^8 \, h^{-1} \, \mathrm{M_\odot}$ play an important role in causing flux anomalies; such low-mass subhaloes have been unresolved in previous studies. There is large scatter in the predicted flux ratios between different haloes and between different projections of the same halo. In some cases, the frequency of predicted anomalous flux ratios is comparable to that observed for the radio lenses, although in most cases it is not. The probability for the simulations to reproduce the observed violations of the cusp lenses is $\approx 10^{-3}$. We therefore conclude that the amount of substructure in the central regions of the Aquarius haloes is insufficient to explain the observed frequency of violations of the cusp–caustic relation. These conclusions are based purely on our dark matter simulations which ignore the effect of baryons on subhalo survivability.

Key words: gravitational lensing – galaxies: elliptical and lenticular, cD – galaxies: formation – dark matter.

1 INTRODUCTION

Currently there are ~ 200 known galaxy-scale lenses, divided roughly equally in number into lensed active galactic nuclei[1] and lensed background galaxies (Bolton et al. 2008). These galaxy-scale lenses allow diverse applications (see the review 'Strong Gravitational Lensing' by Kochanek in Schneider, Kochanek & Wambsganss 2006) such as a determination of the Hubble constant, a characterization of galaxy evolution and measurements of the mass distribution in galaxies. The last application will likely be the

most important one in the next decade, since there are few other probes at intermediate redshifts ($z \sim 0.5$–1).

It was noted quite early on that the flux ratios of the multi-lensed images are more difficult to reproduce with simple parametric mass models than the image positions (Kochanek 1991). This has been termed the 'anomalous flux ratio' problem. Image positions and magnifications (flux ratios) are determined by the first- and second-order derivatives of the lensing potential, respectively. Therefore, flux ratios, as a high-order derivative, are expected to be more sensitive to small changes in the lensing potential than image positions.

In this regard, gravitational lenses with two or three close images deserve special attention because, in these cases, the sources must be close to either a fold or a cusp of the caustic. It is well known for

---

[*]E-mail: Dandan.Xu@postgrad.manchester.ac.uk
[1]http://www.cfa.harvard.edu/castles/

any smooth lensing potential that the close images follow *asymptotic* flux ratio relations: for a close pair, their flux ratio approaches unity when their separation goes to zero, while for a close triple, the ratio of the flux of the middle image to the sum of the fluxes of the two outer images asymptotically goes to unity (Mao 1992; Schneider & Weiss 1992; Keeton, Gaudi & Petters 2003; Congdon, Keeton & Nordgren 2008). However, the observed lensing systems often violate these asymptotic relations. This was taken to be evidence for substructure in lensing galaxies (Mao & Schneider 1998; Metcalf & Madau 2001; Chiba 2002; Dalal & Kochanek 2002; Metcalf & Zhao 2002; Kochanek & Dalal 2004) on the physical scale of the separation between close images (typically of the order of ∼1 kpc). Spectroscopic observations go beyond simple broad-band flux ratios and provide a promising way to probe substructure in lenses (Metcalf et al. 2004; Chiba et al. 2005; Sugai et al. 2007). Other suggestive evidence for substructures comes from astrometry (see Chen et al. 2007 for a general discussion), such as bent jets (Metcalf 2002) and detailed image structures for B2016+112 (Koopmans et al. 2002; Schneider et al. 2006; More et al. 2009) and B0128+437 (Biggs et al. 2004; Zhang 2008). Substructures may also have detectable effects on the time delays in gravitational lenses (Keeton & Moustakas 2009).

Evans & Witt (2003) argued that some of these lensing 'anomalies' may be accommodated by changes in the potentials of the main lensing galaxies in parametric models. However, significant changes are needed in order to explain the anomalies (Kochanek & Dalal 2004; Congdon & Keeton 2005). The angular structures of the lenses whenever the measurements are available suggest ellipsoidal central potentials, where the high-amplitude, higher order multipoles that are required to explain the flux ratio anomalies are not seen (Kochanek & Dalal 2004; Yoo et al. 2005, 2006). There are strong hints that substructures may indeed be real in lensing galaxies. First, observationally, saddle (negative-parity) images are often fainter than the predictions of simple smooth models. This is expected from lensing by substructure (such as stars or subhaloes; Schechter & Wambsganss 2002; Kochanek & Dalal 2004), but impossible to explain by propagation effects, such as galactic scintillation and scatter broadening, as earlier postulated (Koopmans et al. 2003). This arguably constitutes the most convincing evidence for substructure lensing. Secondly, in many gravitational lenses, the substructure is directly seen as luminous satellites. For example, nearly half of the CLASS (the Cosmic Lens All-Sky Survey) lenses (Browne et al. 2003; Myers et al. 2003; Jackson, in preparation) show luminous satellite galaxies within a few kpc of the primary lensing galaxies.[2] Inclusion of satellites in the modelling dramatically improves the fit to the image positions. In the case of B2045+265, the inclusion of a companion galaxy helps to explain the flux ratio anomaly (McKean et al. 2007). The additional dark subhaloes within the main lensing galaxies, as well as the intergalactic perturbers along the line-of-sight (Chen, Kravtsov & Keeton 2003; Wambsganss, Bode & Ostriker 2005; Metcalf 2005a,b; Miranda & Macciò 2007) may also help to explain the observed lensing anomalies.

Much of the interest in (milli-)lensing flux anomalies arises because they may be caused by the elusive substructure generically predicted by the hierarchical structure formation in the cold dark matter (CDM) cosmology (e.g. Kauffmann, White & Guiderdoni 1993; Klypin et al. 1999; Moore et al. 1999; Ghigna et al. 2000; Gao

et al. 2004a,b; Diemand, Kuhlen & Madau 2007). In this model, large structures form via merging and accretion of smaller structures. The cores of these small structures often survive tidal destruction and manifest themselves as subhaloes (substructure). Recent high-resolution simulations predict many thousands of subhaloes (down to $m_{sub} \sim 10^6$ M$_\odot$, or to circular velocity of $V_c \sim 4$ km s^{-1}; e.g. Madau, Diemand & Kuhlen 2008; Springel et al. 2008), at least two orders of magnitude more than the number of observed satellite galaxies in the Milky Way, even after accounting for the newly discovered faint satellite galaxies from the Sloan Digital Sky Survey (Belokurov et al. 2007). A possible solution is that the star formation may be strongly suppressed in the vast majority of the low-mass subhaloes (e.g. Efstathiou 1992; Kauffmann, White & Guiderdoni 1993; Thoul & Weinberg 1996; Bullock, Kravtsov & Weinberg 2000; Gnedin 2000; Benson et al. 2002), and thus they remain dark and difficult to detect through light-based methods. If this is the case, then gravitational lensing can potentially probe this population since it depends only on the mass but not on whether the lenses are luminous or dark.

Numerical simulations indicate that subhaloes typically account for 5–10 per cent of the total mass in a galaxy-type halo (e.g. Klypin et al. 1999; Moore et al. 1999; Ghigna et al. 2000). The study by Dalal & Kochanek (2002) requires $f_{sub} = 0.6$ to 7 per cent (with a median of 2 per cent) of the mass to be in substructures (90 per cent confidence limit) in order to explain the observed flux anomaly problem. At first sight, the fraction of substructure from simulations seems to be more than sufficient to explain the flux anomaly. Upon closer examination, however, a problem emerges: lensing probes the central few kpc around the line-of-sight through the galaxy, while most substructures are in the outer regions of its dark matter halo, since those that come close to the centre are tidally destroyed. Thus, it remains unclear whether the predicted substructure in the inner regions is sufficient or not to explain the observed flux anomalies (e.g. Bradač et al. 2004; Mao et al. 2004; Amara et al. 2006; Macciò & Miranda 2006). In contrast, on cluster scales, the amount of predicted substructure seems to be consistent with weak and strong lensing data (Natarajan, De Lucia & Springel 2007).

Previous lensing studies simulated galaxy-sized haloes with ∼10^6 particles so that subhaloes were resolved down to ∼10^7 to 10^8 h^{-1} M$_\odot$. State-of-the-art simulations can now resolve haloes with two or even three orders of magnitude more particles, thus reaching substantially lower mass subhaloes. In this work, we revisit the issue of substructure lensing using the Aquarius simulations of six galaxy-sized haloes. These collisionless *N*-body simulations were performed by the Virgo Consortium in a concordance ΛCDM universe. The subhaloes in each halo are resolved down to masses of $m_{sub} \sim 10^5$ h^{-1} M$_\odot$ (Springel et al. 2008), at least two orders of magnitude better than that in previous substructure lensing studies.

Our paper is organized as follows. In Section 2, we describe the realization and the properties of the simulated lensing galaxies. Our methods and techniques for the lensing simulations together with our test results are presented in Section 3. In Section 4, we apply our lensing simulation to the six simulated galaxy haloes from the Aquarius simulation to derive their lensing properties, including the cusp relations, and we compare the numerical results with observations. A summary of the paper and a discussion are given in Section 5. The cosmology we adopt for the lensing simulation is the same as that used for the Aquarius simulations (Springel et al. 2008), with a matter density $\Omega_m = 0.25$, cosmological constant $\Omega_\Lambda = 0.75$, Hubble constant $h = H_0/(100$ km s^{-1} Mpc$^{-1}) = 0.73$ and linear fluctuation amplitude $\sigma_8 = 0.9$.

---

[2] This fraction is a factor of ∼2 higher than that claimed in Bryan, Mao & Kay (2008) as revealed by a more careful analysis of Hubble Space Telescope (*HST*) images of the CLASS lenses (Jackson, in preparation).

Table 1. Dark matter halo properties in the Aquarius simulations.

Halo name	r_{200} (h^{-1} kpc)	M_{200} ($10^{10} h^{-1}$ M$_\odot$)	c	Mass resolution (h^{-1} M$_\odot$)	N_{200}	N_{sub}	f_{sub} (per cent)
Aq-A-2	179.5	132.8	16.2	1.0×10^4	1.3×10^8	2.1×10^4	7.14
Aq-B-2	137.1	59.5	9.7	4.7×10^3	1.3×10^8	2.5×10^4	6.98
Aq-C-2	177.3	127.7	15.2	1.0×10^4	1.2×10^8	1.7×10^4	4.12
Aq-D-2	177.3	128.5	9.4	1.0×10^4	1.3×10^8	2.2×10^4	6.56
Aq-E-2	155.0	85.7	8.3	7.0×10^3	1.2×10^8	2.3×10^4	7.28
Aq-F-2	153.0	80.5	9.8	4.9×10^3	1.6×10^8	2.6×10^4	11.20
Aq-A-2 ($z = 0.6$)	134.4	92.2	10.4	1.0×10^4	9.3×10^7	1.7×10^4	6.50

Note. Column 1: halo name, Columns 2–4: r_{200}, c and M_{200} are defined in equation (1) for the main halo. Column 5: mass resolution (h^{-1} M$_\odot$). Column 6: N_{200} is the total number of particles within r_{200}. Column 7: N_{sub} is the number of subhaloes within r_{200}. Column 8: f_{sub} is the mass fraction of subhaloes within r_{200}, defined by M_{sub}/M_{tot}.

2 FROM DARK MATTER HALOES TO EARLY-TYPE LENSING GALAXIES

In this section, we summarize the properties of dark matter haloes from the Aquarius simulations relevant to our study, in particular the subhalo properties. Readers are referred to Springel et al. (2008) for more details. We will show that dark matter alone is, as expected, insufficient to cause multiple image splittings, and therefore we must incorporate a stellar component; we detail such a procedure in Section 2.2.

2.1 The Aquarius simulations

The Aquarius project (Springel et al. 2008) is a suite of simulations of six galaxy-sized dark matter haloes with five levels of numerical resolution. The haloes were selected from a $100 \, h^{-1}$ Mpc simulation box within the concordance cosmology (for parameters see above). The simulations were run with GADGET-3, an improved version of the GADGET-2 code (Springel, Yoshida & White 2001; Springel 2005). The highest resolution level (level 1) was achieved for only one halo ('Aq-A-1') with ~1.5 billion halo particles. Level-2 simulations were performed for a sample of six dark matter haloes, with about 200 million particles per halo. The softening length is ~$0.05 \, h^{-1}$ kpc, and the mass resolution ranges from 10^3 to $10^4 \, h^{-1}$ M$_\odot$. All haloes are Milky Way-type systems in terms of their masses and rotation curves. We will use the six level-2 haloes (*Aq-A-2*, *Aq-B-2*, *Aq-C-2*, *Aq-D-2*, *Aq-E-2* and *Aq-F-2*) at redshift zero for our analysis of substructure lensing. As we will show later on, the scatter in lensing properties among different haloes (and for different projections) is large, and so it is important to examine more than one halo for statistical purposes.

The basic properties of the six haloes at $z = 0$ are listed in Table 1. In particular, all the density profiles are reasonably fit by Navarro, Frenk and White (NFW) profiles (Navarro, Frenk & White 1996; Navarro, Frenk & White 1997):[3]

$$\rho(r) = \frac{M_{200}}{4\pi r(r + r_{200}/c)^2 f(c)},$$

$$M(<r) = \frac{M_{200} f(r \, c/r_{200})}{f(c)},$$

$$f(c) = \ln(1 + c) - c/(1 + c), \tag{1}$$

---

[3] An even better fit is found using the Einasto (1965) profile (Navarro et al. 2008), but here we adopt the simpler NFW profile which we use later to take into account the adiabatic contraction of dark matter haloes.
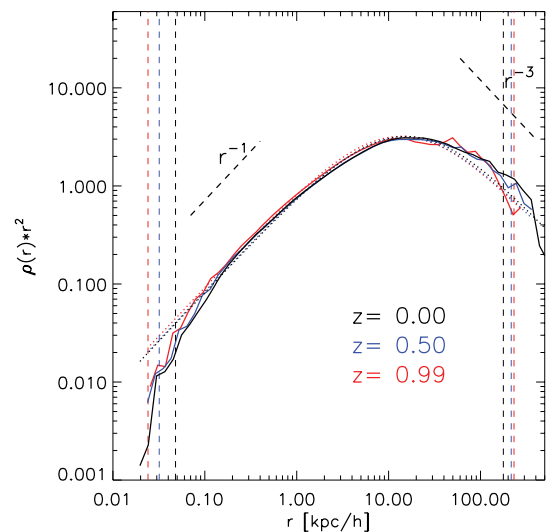

Figure 1. Density profiles (solid curves), multiplied by r^2, for the halo *Aq-D-2* at redshifts $z = 0$, 0.5 and 0.99. All haloes are reasonably well fitted by the NFW profile (dotted curves, see equation 1), which follows $\rho(r) \propto r^{-1}$ on small scales and $\rho(r) \propto r^{-3}$ on large scales. The vertical dashed lines indicate the softening length and r_{200}.

where r_{200} is the radius within which the mean dark halo mass density is 200 times the critical density, M_{200} is the mass enclosed within r_{200} and $c \equiv r_{200}/r_s$ is the concentration parameter with r_s being the scale radius.

We artificially put all these haloes (snapshot $z = 0.0$) at redshift $z = 0.6$ (corresponding roughly to the most likely lens redshift; e.g. Turner, Ostriker & Gott 1984), keeping their physical sizes unchanged. However, we also take a snapshot of the halo *Aq-A-2* at redshift $z = 0.6$ as a lens, and compare its lensing properties with those artificially shifted to $z = 0.6$. As will be shown in Section 4, the scatter among the six haloes is much larger than the differences between haloes at redshifts $z = 0$ and 0.6, and so adopting the $z = 0$ haloes will not significantly change the properties of substructure lensing. This is also seen in the evolution of density profiles of these haloes. Fig. 1 shows the density profiles for the halo *Aq-D-2* at redshifts 0, 0.50 and 0.99. The changes in the profiles since redshift 1 are relatively small since the Aquarius haloes form earlier than that.

As we are primarily interested in the substructure lensing, an important step is the identification of the subhaloes. We use the
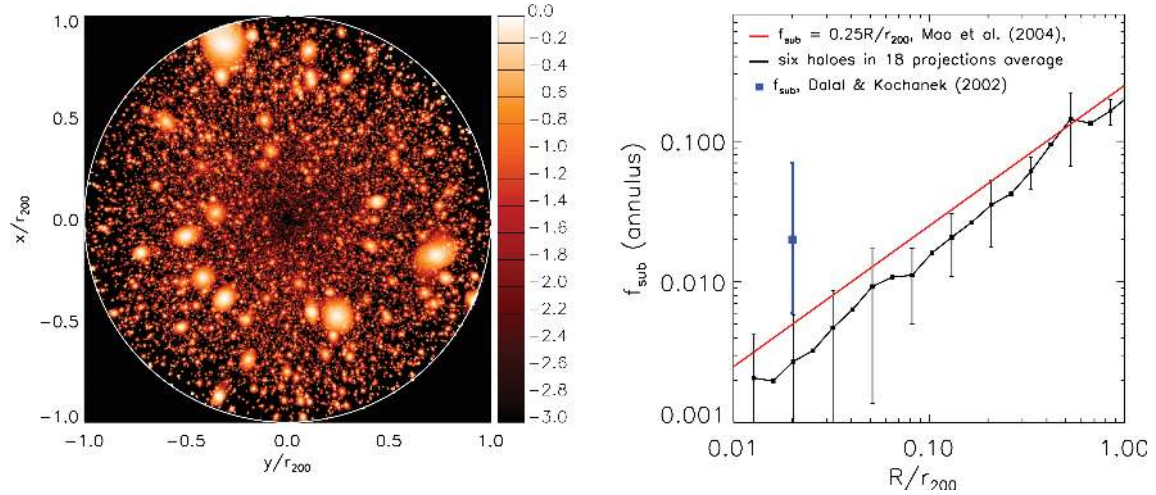
Figure 2. The left-hand panel shows a contour map of the subhalo surface mass density fraction, which is the ratio of the surface mass in subhaloes to that in the total halo, for *Aq-D-2* projected along the *Y*-axis. The right-hand panel shows the mean distribution of subhalo surface mass fraction as a function of R/r_{200}, averaged over the three independent projections of each of the six Aquarius haloes at redshift $z = 0$. The error bars indicate the 68 per cent scatter among different projections and haloes. The red lines show the fit from Mao et al. (2004). The blue point indicates the median and 90 per cent confidence level of the required fraction found by Dalal & Kochanek (2002) (assuming the Einstein radius to be 0.02 r_{200}).

SUBFIND routine (Springel 2005) to identify subhaloes exceeding 20 particles, which corresponds to a minimum subhalo mass of $\sim 10^5 \, h^{-1} \, \mathrm{M_\odot}$. The number of subhaloes in each halo ranges from about 1.7×10^4 to 2.6×10^4 within r_{200}, with 4.1–11.2 per cent of the total halo mass locked up in bound subhaloes (see Column 8: f_{sub} in Table 1).

The subhalo mass function follows a power law: $\mathrm{d}N(m_{\mathrm{sub}})/\mathrm{d}m_{\mathrm{sub}} \propto m_{\mathrm{sub}}^{-1.9}$ (Springel et al. 2008). The average mass of subhaloes (within r_{200}) is $\sim 10^6$ to $10^7 \, h^{-1} \, \mathrm{M_\odot}$ and their average half-mass radius is $\leq 0.2 \, h^{-1} \, \mathrm{kpc}$, with large scatter. The most massive subhalo has a mass of $\sim 10^9$ to $10^{10} \, h^{-1} \, \mathrm{M_\odot}$ and a half-mass radius ~ 5–$10 \, h^{-1} \, \mathrm{kpc}$.

As an example, we again consider halo *Aq-D-2* and show in the left-hand panel of Fig. 2 the *Y*-projection of the surface mass fraction in subhaloes within r_{200}. The right-hand panel in the same figure shows the surface mass fraction of subhaloes averaged within azimuthal annuli as a function of the normalized radius R/r_{200}. It is clear that the scatter in the projected mass fraction of subhaloes among different haloes is large. Within 0.1 r_{200}, the mean fraction is ~ 0.005, with a scatter of a factor of 10. The red line in the same panel shows the result from Mao et al. (2004), which was obtained from 12 haloes (of galactic, group and cluster masses) and 30 random projections. Their result lies somewhat higher than found here although still within the scatter. This is probably due to the inclusion of group- and cluster-sized haloes in the averaging, which tend to have a higher substructure fraction due to their later formation times. The blue point indicates the required substructure mass fraction found by Dalal & Kochanek (2002) to be 0.02 (median, ranging from 0.006 to 0.07 at 90 per cent confidence).

2.2 Adding 'light' to dark matter haloes

We put the source redshift z_s at 3.0. This is reasonable since many lensed quasars are at similar redshift. The lensing critical surface density is given by

$$\Sigma_{\mathrm{cr}} = \frac{c^2}{4\pi G} \frac{D_\mathrm{s}}{D_\mathrm{d} D_{\mathrm{ds}}}, \tag{2}$$

where D_s, D_d and D_{ds} are the angular diameter distances between the source and the observer, the lens and the observer, and the source and the lens, respectively. For our adopted source and lens redshifts, $\Sigma_{\mathrm{cr}} = 1.82 \times 10^9 \, \mathrm{M_\odot \, kpc^{-2}} = 7.95 \times 10^{10} \, \mathrm{M_\odot \, arcsec^{-2}}$.

To produce multiple images, the maximum surface density of a halo usually has to be super-critical. The left-hand panel of Fig. 3 shows the surface density distribution for the halo *Aq-D-2* projected along the *Y*-axis. Clearly, the central surface density of the (initial) NFW dark matter halo is below the critical value, and thus generally no multiple images can be produced (e.g. Williams, Navarro & Bartelmann 1999; Rusin & Ma 2001). This is hardly surprising, since for galaxy-scale strong lensing, the images form only a few kpc (projected) from the centre where baryons play a crucial role. Thus, one must incorporate a baryonic component in order to model the lensing galaxy more realistically, a topic we turn to next.

Most gravitational lenses are early-type (elliptical) galaxies rather than late-type (disc) galaxies, as the former are more massive and dominate the lensing cross-sections (Turner et al. 1984). There have been many hybrid models used for the lensing galaxies (e.g. Keeton 2001; Kochanek & White 2001; Oguri 2002; Jiang & Kochanek 2007). We use the spherical Hernquist profile to model the light distribution, since it approximates the de Vaucouleur's profile that has been observed for elliptical galaxies and bulges, and it has many known, convenient analytical properties.

The three-dimensional (3D) density and mass profiles $\rho_\mathrm{H}(r)$, $M_\mathrm{H}(r)$ for the Hernquist distribution are given by (Hernquist 1990)

$$\rho_\mathrm{H}(r) = \frac{a M_\star}{2\pi r} \frac{1}{(r + a)^3},$$

$$M_\mathrm{H}(<r) = M_\star \frac{r^2}{(r + a)^2}, \tag{3}$$

where $M_\star$ is the total baryonic mass and a is a scale length related to the effective spherical radius r_e (within which half of the mass is contained) by $a = r_\mathrm{e}/(\sqrt{2} + 1)$.

The profile is specified by two parameters a (or r_e) and $M_\star$, which are linked with the dark matter halo parameters r_{200} and M_{200}
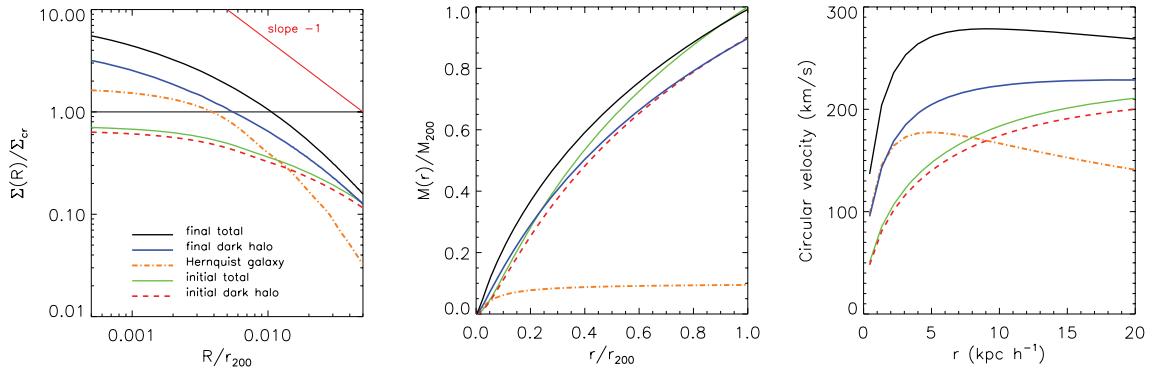
Figure 3. The halo *Aq-D-2*: the left-hand panel shows the surface density profiles $\Sigma(R)$ projected in the Y-direction, and normalized to the critical surface density. Profiles are for cases before and after adding a Hernquist galaxy and the dark matter halo's adiabatic contraction, assuming the added baryonic component has 10 per cent of the total mass and an effective radius of 5 per cent of the halo virial radius ($f_\star = 0.1$, $f_{re} = 0.05$). Line symbols are labelled inside the figure. The isothermal slope [$\Sigma(R) \propto R^{-1}$] is indicated by the red line at the top right (see Section 2.2 for details). The middle panel shows the mass distributions $M(\leq r)$. The right-hand panel shows the rotation curves $V_c(r)$. The final total rotation curve is flat from $\sim 5\,h^{-1}$ kpc out to a few tens of kpc.

by

$$f_{re} = \frac{r_e}{r_{200}}, \quad f_\star = \frac{M_\star}{M_{200}}, \quad M_{200} = M_{DM} + M_\star. \quad (4)$$

Note that the mass of the main halo dark matter M_{DM} is reduced by a factor of $(1 - f_\star)$ to conserve the total mass and the mass of substructures.

The inclusion of the baryonic component affects the distribution of the dark matter halo. Many studies have shown that the adjustment of the dark matter halo can be approximated by an adiabatic contraction (Barnes & White 1984; Blumenthal et al. 1986). Gnedin et al. (2004) have proposed a modification to this simple model in order to take into account the fact that particle orbits in realistic haloes are not circular, but it is not clear whether this modification is able to reproduce accurately the results of numerical simulations (see, e.g. Abadi et al. 2009). In view of this, we have decided to follow, for simplicity, the procedure outlined by Mo, Mao & White (1998). Assuming that both the baryon and dark matter components follow an NFW distribution initially, baryons ($f_\star$ per cent of the total matter) then cool to form the galaxy at the centre, which causes the dark matter halo to contract adiabatically. After the adiabatic contraction, the dark halo follows a new profile and hosts a Hernquist galaxy at its centre. Note that we contract all the particles in different components (i.e. diffuse dark matter and subhaloes) in the same way.

The two parameters (f_{re} and $f_\star$) are chosen according to two criteria (after adding the baryonic galaxy and accounting for the adiabatic contraction): (i) the projected dark matter mass fractions inside the Einstein radii of the host galaxy haloes should range from 0.4 to 0.7 (Treu & Koopmans 2004); (ii) the projected slopes are close to isothermal at a few kpc from the galactic centre (e.g. Rusin, Kochanek & Keeton 2003; Rusin & Kochanek 2005; Koopmans et al. 2006; Gavazzi et al. 2007), or equivalently, the final rotation curves are roughly flat from a few kpc out to a few tens of kpc (see Fig. 3). Furthermore, $f_\star$ should be smaller than the universal baryonic fraction of $\sim$17.5 per cent (from *WMAP*-3, Spergel et al. 2007).

We find that $f_{re} = 0.05$ and $f_\star = 0.1$ satisfy these criteria well. From Fig. 3 (the left-hand panel), it is clearly seen that after inserting the baryonic galaxy and taking the adiabatic contraction into account, the total surface density is now super-critical and the corresponding Einstein radius is of the order of a few kpc, similar to

that in many gravitational lenses. Note, however, that our procedure is not self-consistent dynamically, since the inclusion of a baryonic component will affect the evolution and survival of subhaloes. We shall return to this point briefly in the discussion.

3 LENSING METHODOLOGY

N-body simulations provide us with the positions (and velocities) of particles. For lensing calculations, we first project the particles on to a mesh in the lens plane (and tabulate the stellar surface density), and then smooth the surface density field appropriately. Using the smoothed surface density map, we can numerically calculate the lensing potential, deflection angles and magnifications. The details of the numerical procedure are given in Section 3.1.

We test the accuracy of our numerical procedure by comparing with known analytical results, using a singular isothermal sphere realized through Monte Carlo simulations in Section 3.2. We then relax the spherical assumption, and further test our procedure with an isothermal ellipsoid (IE) generated with a similar number of particles as those in the Aquarius simulations; the comparison results are presented in Section 3.3.

3.1 From particles to lensing images

3.1.1 Coarse and fine particle meshes

We use a Particle-Mesh (PM) code for the lensing potential calculation. The application of fast Fourier transforms (FFT) in the PM algorithm makes it computationally efficient. However, it is limited in resolution by the finite mesh size and so cannot accurately represent regions with rapid density variations on the scale of the grid size. To increase the accuracy in the regions of interest (within a few kpc from the centres of galaxies), we establish two two-dimensional (2D) meshes: a coarse grid used for the potential field generated by the mass projected outside the central $(20\,h^{-1}\,\text{kpc})^2$ region, and a fine grid for the mass within. Both grids have 1024×1024 pixels, covering $(4\,r_{200})^2$ and $(40\,h^{-1}\,\text{kpc})^2$ (see Section 3.1.3) with resolutions $\sim$0.6 and $0.04\,h^{-1}$ kpc for the coarse and fine grids, respectively (the factor of 2 increase in the box size is due to the isolated boundary condition, see Section 3.1.3). This resolution ensures that the tangential critical curves are resolved with sufficient accuracy. In contrast, the inner radial critical curves may not be

well reproduced, due to the finite resolution of the mesh. However, this is not a major concern since all the bright images that we are interested in form close to the outer (tangential) critical curves. Furthermore, the resolution of the fine mesh is similar to the softening length of the simulations, and the density distributions in the very central regions are not accurately modelled in the simulations on scales smaller than the gravitational softening in the first place.

3.1.2 Particle assignment with smoothed particle hydrodynamics kernel

The surface density maps of the Aquarius haloes are obtained by assigning particles to the potential meshes using the smooth particle hydrodynamics (SPH) kernel (Monaghan 1992). Although, in the end, we will approximate the underlying mass distributions of the Aquarius haloes by IEs in order to circumvent problems caused by discreteness noise (see Section 3.3), SPH-smoothed density fields are used as an intermediate step to generate basic lensing properties (e.g. critical curves and caustics) to constrain the best-fitting IEs. For more detail, see Section 4.

The advantage of the SPH assignment is that it adjusts the smoothing scale according to the local density environment: particles in a high-density region are mildly smoothed while those in a low-density region are smoothed more. For each particle, a smoothing length $\mathcal{H}$ is calculated according to the local number density in its 3D neighbourhood. The particle mass is then assigned to all the mesh cells that are within a circle of $2\mathcal{H}$ in radius in its neighbourhood. The 3D density kernel can be integrated along the line-of-sight analytically to obtain the surface density distribution:

$$\Sigma(u) = \frac{1}{\pi\mathcal{H}^2} \begin{cases} \frac{1}{16}[-(8+52u^2)\sqrt{1-u^2}+(16+26u^2)\sqrt{4-u^2} \\ \quad -9u^4\ln u + 3u^2(16+4u^2)\ln(1+\sqrt{1-u^2}) \\ \quad -3u^2(16+u^2)\ln(2+\sqrt{4-u^2})], \quad \text{if } 1 > u \geq 0 \\ \frac{1}{16}[2\sqrt{4-u^2}(8+13u^2)+3u^2(16+u^2)\ln u \\ \quad -3u^2(16+u^2)\ln(2+\sqrt{4-u^2})], \quad \text{if } 2 > u \geq 1 \\ 0, \quad \text{if } u > 2 \end{cases} \tag{5}$$

where $u \equiv r/\mathcal{H}$ is the distance from the cell centre to the particle normalized to $\mathcal{H}$, and the total mass within $u \leq 2$ is unity.

The smoothing length $\mathcal{H}$ for each particle depends on its local density and is controlled by the parameter N_{ngb}, the number of particles that are contained within radius $\mathcal{H}$. A good smoothing procedure should reduce the numerical noise without smoothing excessively out the real density fluctuations (e.g. substructures).

The total mass that has been assigned to the neighbouring cells should be equal to the mass of the particle. However, this is only approximately true due to the discreteness of cells. In particular, mass conservation is quite poorly observed when the smoothing length $\mathcal{H}$ is only a few mesh cells, which may happen in a dense environment. For particles with $2\mathcal{H} \leq 15$ cell sizes (30 cells in diameter), we therefore renormalize each individual kernel so that the total mass is conserved during the assignment.

We find in practice that SPH assignment is superior to Cloud-In-Cell (CIC) assignment in terms of reducing discreteness noise. For a singular isothermal sphere realized with 10^6 particles, the SPH-smoothed ($N_{ngb} = 32$) and CIC-smoothed surface density fields show fluctuations of 2 and 30 per cent relative to the analytical results, respectively. For a realization with 10^7 particles, the fluctuations decrease to 1 per cent for the SPH assignment ($N_{ngb} = 320$,

with the same smoothing length, $\mathcal{H} \propto N_{p}^{-1/3} N_{ngb}^{1/3}$; Li et al. 2006) and to 10 per cent for the CIC assignment.

3.1.3 Isolated boundary conditions

Periodic boundary conditions are most natural for Fourier transforms, but are not appropriate for lensing galaxies. We follow Hockney & Eastwood (1981) to eliminate the (aliasing) effects due to 'mirror' particles by using a mesh twice as big as the simulated lens system to assign particles, padding the region outside the simulation volume with zeros. A truncated 2D gravitational force kernel is tabulated on to a simulation mesh same in size, and then convolved with the assigned surface density field. The gravitational effect is accurately reproduced within the region where the mass has been distributed (see Hockney & Eastwood 1981, for more technical details). We adopt this procedure throughout this work.

3.1.4 Lensing potential, deflection angle and magnification

After the discretization of the surface density field through SPH assignment and the tabulation of the truncated 2D gravitational kernels on the meshes, the potentials and their derivatives are easily calculated by convolutions which can be efficiently implemented in Fourier space through FFT.

In particular, the effective lensing potential $\psi(\boldsymbol{\theta})$ is the convolution of the surface density $\Sigma(\boldsymbol{\theta})$ and the 2D kernel $\ln|\boldsymbol{\theta}|$:

$$\psi(\boldsymbol{\theta}) = \frac{1}{\pi} \int \Sigma(\boldsymbol{\theta}') \ln|\boldsymbol{\theta} - \boldsymbol{\theta}'| \, d^2\theta'. \tag{6}$$

The deflection angle $\boldsymbol{\alpha}(\boldsymbol{\theta})$ is the first derivative of the lensing potential, $\psi(\boldsymbol{\theta})$, and is thus the convolution of the surface density $\Sigma(\boldsymbol{\theta})$ and the 2D force kernel $\boldsymbol{\theta}/|\boldsymbol{\theta}|^2$:

$$\boldsymbol{\alpha}(\boldsymbol{\theta}) \equiv \nabla\psi(\boldsymbol{\theta}) = \frac{1}{\pi} \int \Sigma(\boldsymbol{\theta}') \frac{\boldsymbol{\theta} - \boldsymbol{\theta}'}{|\boldsymbol{\theta} - \boldsymbol{\theta}'|^2} \, d^2\theta'. \tag{7}$$

The convergence $\kappa(\boldsymbol{\theta})$ (the surface density normalized to Σ_{cr}) and the shear $\gamma(\boldsymbol{\theta})$ are second-order derivatives of the lensing potential $\psi(\boldsymbol{\theta})$:

$$\kappa = (\psi_{11} + \psi_{22})/2, \quad \gamma_1 = (\psi_{11} - \psi_{22})/2,$$

$$\gamma_2 = \psi_{12} = \psi_{21}, \quad \gamma^2 = \gamma_1^2 + \gamma_2^2, \quad \psi_{ij} \equiv \frac{\partial^2\psi}{\partial\theta_i\,\partial\theta_j}, \tag{8}$$

where the derivatives are taken with respect to the index 1 (x) and 2 (y). Numerically, the convergence and shear can be calculated through fourth-order finite differencing from the deflection angle $\boldsymbol{\alpha}(\boldsymbol{\theta})$. The magnification $\mu(\boldsymbol{\theta})$ is related to the convergence and shear by

$$\mu = \frac{1}{(1-\kappa)^2 - \gamma^2}. \tag{9}$$

3.1.5 Image finding and cusp relation

Since all the lensing quantities are now known, it is straightforward to find the images for any given source position. To this end, we construct a separate mesh in the image plane, with a resolution (0.02 h^{-1} kpc) higher than the fine potential mesh discussed in Section 3.1.1; the lensing properties (deflection angle, magnification, etc.) on this ultra-fine mesh are found through bilinear interpolation. We then search image positions (and magnifications) using the Newton–Raphson and triangulation methods (Schneider, Ehlers & Falco 1992).

Of particular interest to gravitational lensing are the critical curves and caustics. Critical curves in the image plane are a set of points where the magnification is formally infinite for a point source, $\mu(\boldsymbol{\theta}) \longrightarrow \infty$. In practice, they are identified according to the fact that the magnifications have different signs (i.e. different parities) for images on different sides of a critical curve. Critical curves are mapped into caustics in the source plane, which can be easily obtained through the lens equation.

Most strong lenses occur in elliptical galaxies since they have larger lensing cross-sections than spiral galaxies (Turner et al. 1984). They typically form two distinct sets of critical curves and corresponding caustics: the tangential ('outer') and radial ('inner') critical curves, which are mapped into tangential ('inner') and radial ('outer') caustics (see Fig. 5 for an example). A source inside the central caustic usually produces five images: four close to the tangential critical curve and one central image which is usually too faint to be observable (and is of no interest to us for the present work).

We are particularly interested in sources that are close to the cusps of the tangential caustic ('cusp sources'). For cusp sources, three close images form around the tangential critical line, with alternate parities. There are two different kinds of cusp sources and corresponding image configurations. As illustrated in Fig. 5, a 'major cusp' source forms three images around the tangential critical curve on the same side of the source (with respect to the centre of the lens) while a 'minor cusp' source forms three close images on the opposite side of the source.

In any smooth lensing potential, for a source very close to a cusp, the three close images satisfy an asymptotic magnification relation (the 'cusp–caustic relation'; Blandford & Narayan 1986; Schneider & Weiss 1992; Keeton et al. 2003):

$$R_{\text{cusp}} \equiv \frac{|\mu_A + \mu_B + \mu_C|}{|\mu_A| + |\mu_B| + |\mu_C|} \to 0, \tag{10}$$

with the total absolute magnification $|\mu_A| + |\mu_B| + |\mu_C| \to \infty$.

For each of the cusp sources, we define an image opening angle $\Delta\theta$, ranging from 0 to π, which measures the angle (from the lens centre) of the outer images of the close triple. Note that both $\Delta\theta$ and R_{cusp} are observable. In a smooth lens potential, as a source moves to a cusp caustic, both $\Delta\theta$ and R_{cusp} decrease asymptotically to zero. As can be seen from Fig. 6, there are two leading patterns on the $R_{\text{cusp}} - \Delta\theta$ diagram due to 'major' and 'minor' cusp sources. Generally speaking, the major cusp sources have larger R_{cusp} than the minor cusp sources for the same image opening angle.

The cusp–caustic relation predicts that in smooth lens models R_{cusp} would asymptotically approach zero when a source moves towards the caustic. However, the presence of (clumpy) substructures will break down the smooth potential assumption in the asymptotic cusp–caustic relation, resulting in substantial deviations in R_{cusp} values and other quantities (such as image positions and time delays) from simple predictions. Therefore, the examination of the cusp–caustic relation is a way to test for the presence of substructures that are projected near the (tangential) critical curves. However, caution must be exercised because, even for smooth lens models, a high R_{cusp} is possible. There are many factors that affect the R_{cusp} distribution apart from the presence of substructures, for example, the mass distribution of the lens (radial profile and the ellipticity), external shear from the environment and the selection criteria of the cusp sources (for more discussions see Keeton et al. 2003).

3.2 Singular isothermal sphere

We test our lensing simulation code with Monte Carlo realizations of singular isothermal spheres (SIS), for which analytical lensing properties are known. Each of our SIS contains a mass of $10^{12}\, h^{-1}\, \text{M}_\odot$ within a virial radius of $100\, h^{-1}$ kpc, realized with 10^6 and 10^8 particles; the SPH assignment parameter is chosen to be $N_{\text{ngb}} = 32$ and 640 for the two cases, respectively. Fig. 4 shows the numerical accuracy of the deflection angle, convergence (surface density) and magnification in our numerical procedures. For the 10^6 particle case, two Monte Carlo realizations (cyan and blue curves) are shown. For the 10^8 particle realization, the uncertainties around the Einstein radius [at about 0.02 r_{200}, defined by a total magnification $\mu(\boldsymbol{\theta}) \geq 20$] are 0.2 per cent for the deflection angle, 1 per cent for the convergence and <10 per cent for the lensing magnification (estimated by the half width half maximum of the probability distributions). The deviation towards the centre is due to the fact that the finite mesh resolution of the PM code fails to represent the singular behaviour at the centre of the SIS. The significant deviation of the magnification seen near the Einstein radius is due to the divergent behaviour of the magnification close to the critical curve, where $\mu = 1/[(1-\kappa)^2 - \gamma^2] \longrightarrow \infty$, when $\kappa = \gamma = 0.5$ at the Einstein radius for the singular isothermal sphere.

3.3 High-resolution isothermal ellipsoid

We simulate an IE with 10^6 and 10^8 particles (as in the Aquarius haloes). Such an isothermal ellipsoidal distribution is modelled as an oblate spheroid with axis ratio q_3 and with a density distribution

$$\rho \propto \left(S_0^2 + R^2 + z^2/q_3^2 \right)^{-1}, \tag{11}$$

where S_0 is a core radius and (R, z) are the cylindrical coordinates. It is specified by three parameters (see Keeton & Kochanek 1998 for details): the effective critical radius b_{I}, the eccentricity of the mass distribution $e = (1 - q_3^2)^{1/2}$ and a core radius S_0. The parameters for the isothermal ellipsoidal halo are adjusted so that its critical curves and caustics match those for the halo *Aq-F-2* in the z-projection. The parameters are $b_{\text{I}} = 0.4$ arcsec, $q_3 = 0.8$, $S_0 = 0.1$ arcsec and the major axis of the surface density ellipse is rotated by $\sim \pi/8$ with respect to the *X*-axis.

Fig. 5 shows analytical and numerical critical curves, caustics and R_{cusp} maps for sources located inside the diamond caustics. The two critical curves nearly overlap each other, with barely notable wiggles in the numerical result. The caustics also agree reasonably well for the 10^8-particle case, but for the 10^6-particle realization (blue lines), higher order singularities such as swallowtails are clearly seen close to the cusps and along the fold caustics. These arise due to numerical noise. The numerical R_{cusp} map shows visible distortions compared with the smooth contours in the analytical results, even in the central region.

Fig. 6 presents the R_{cusp} distributions for caustic sources (indicated in the left-hand panel) with image opening angle $\Delta\theta \leq 90°$. The analytical results show two distinct peaks due to major-cusp and minor-cusp sources with a sharp dropoff around $R_{\text{cusp}} \sim 0.12$. In contrast, for the numerical distributions, even the 10^8-particle realization shows a much broader profile than the analytical one, with an extended tail out to $R_{\text{cusp}} \sim 0.4$ due to numerical noise. Note that the numerical noise behaves in a similar way as real substructures in the R_{cusp} distribution.

In the current numerical set-up with $N_{\text{ngb}} = 640$ for a 10^8-particle simulation, the smoothing length $\mathcal{H}$ in the central region (of the halo)
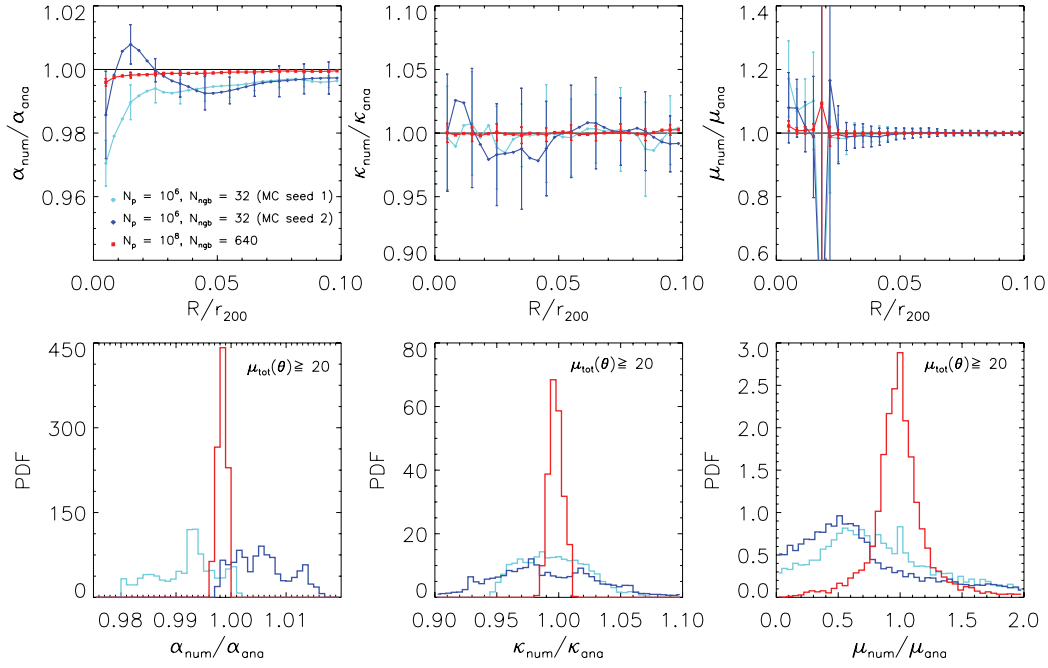
Figure 4. The numerical accuracy of the deflection angle, the convergence and the magnification for Monte Carlo realizations of singular isothermal spheres. The top panels show the ratios of the numerical to the analytical results as a function of radius. The deviation in the numerical magnification (on the right) towards the centre is due to the finite mesh resolution of the PM code, and that seen near the Einstein radius (at about $0.02 r_{200}$) is due to the divergent behaviour of the magnification close to the critical curve. The corresponding probability distributions for images with a total magnification above 20 (around $r \sim 0.02 r_{200}$) are presented in the bottom panels. The cyan and blue curves are for two 10^6-particle realizations (with $N_{ngb} = 32$) while the red curve is for a 10^8-particle realization (with $N_{ngb} = 640$).
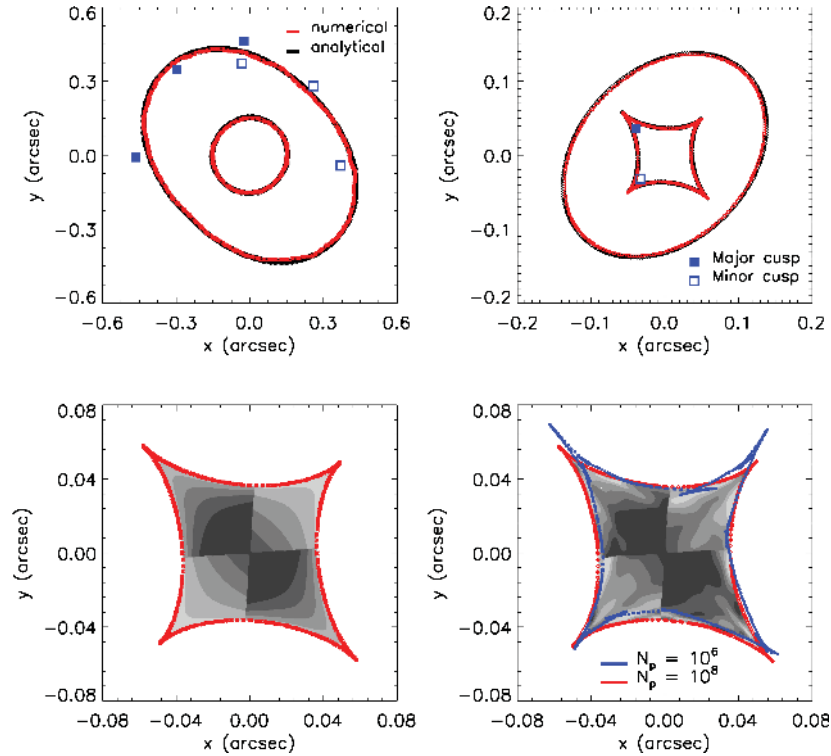
Figure 5. Critical curves, caustics, and cusp–caustic relation R_{cusp} maps for a Monte Carlo realizations of IE with $N_p = 1.6 \times 10^8$ and $N_{ngb} = 640$. The top panels show the critical curves and the caustics. The position and corresponding images are shown for a 'major cusp' (solid squares) and a 'minor cusp' source (open squares). The bottom panels show the R_{cusp} maps from the analytical solution (left) and from the numerical result (right), with contour levels (0.0, 0.05, 0.1, 0.15, 0.2). The numerical tangential caustic from a $N_p = 10^6$ Monte Carlo realization is also presented (blue curve). The swallowtails due to numerical noise are more apparent in this case.
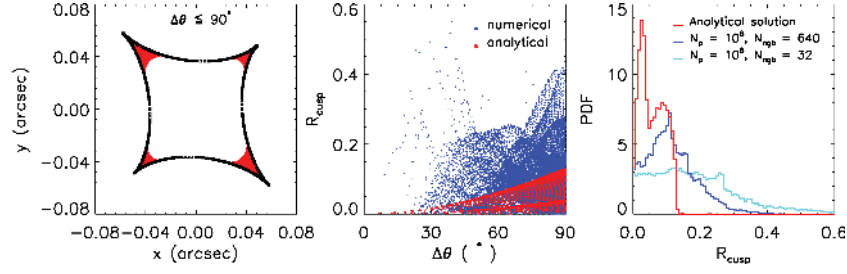
Figure 6. The cusp–caustic relations [of the same Monte Carlo realized isothermal ellipsoidal (IE) halo as in Fig. 5] for caustic sources with image opening angles $\Delta\theta \leq 90°$. The left-hand panel shows the source positions with respect to the tangential caustic. The middle panel shows both the numerical (10^8-particle realization) and analytical results of R_{cusp} versus $\Delta\theta$. The right-hand panel shows the probability density distributions of R_{cusp} for the analytical IE (red), and the two Monte Carlo realized haloes with 10^6 (cyan) and 10^8 particles (blue), respectively.
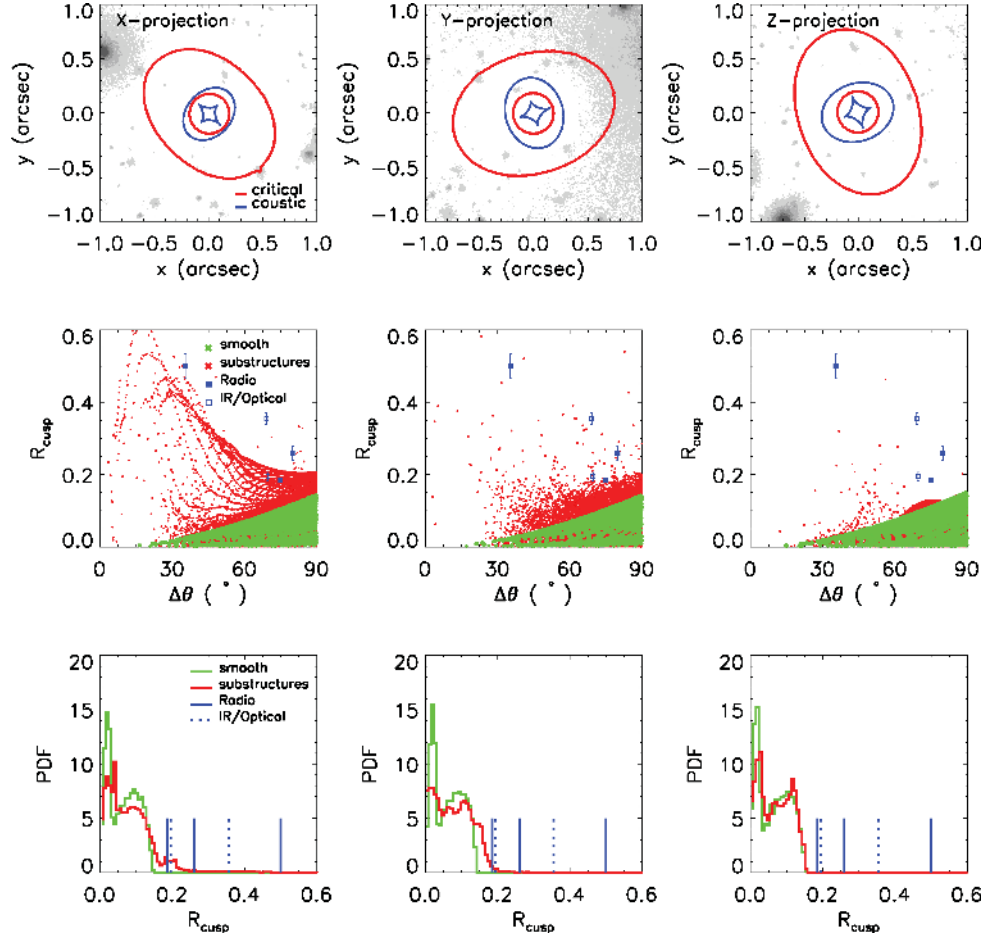
Figure 7. Lensing properties for the halo *Aq-A-2*, in three independent projections. The top panels show the critical curves (red) and caustics (blue) superimposed on top of the subhalo population. The middle panels show R_{cusp} versus the image opening angle $\Delta\theta$. Large R_{cusp} values (red) are due to substructure. The triangle pattern (green) gives predictions for the smooth counterparts. The bottom panels show the corresponding probability distribution functions (PDFs) of R_{cusp} for cusp sources with $\Delta\theta \leq 90°$. The violation of the cusp–caustic relation can be seen from the excess of R_{cusp} at large values (red) over the smooth counterpart curve (green). The R_{cusp} values for the three radio and two optical/IR cusp lenses are indicated by vertical solid and dashed bars (see Table 2).

approximately reaches the softening length of the Aquarius simulation, also roughly the cell resolution of the fine mesh. Increasing $\mathcal{H}$ will indeed further suppress the noise, but it may also over-smooth the underlying density field. Below we outline an alternative way to approximate the smooth underlying density fields for the host galaxy haloes.

4 RESULTS

4.1 Lensing predictions for Aquarius haloes

In this section, we will apply our lensing methodology to the Aquarius haloes (and a baryonic component modelled as a Hernquist
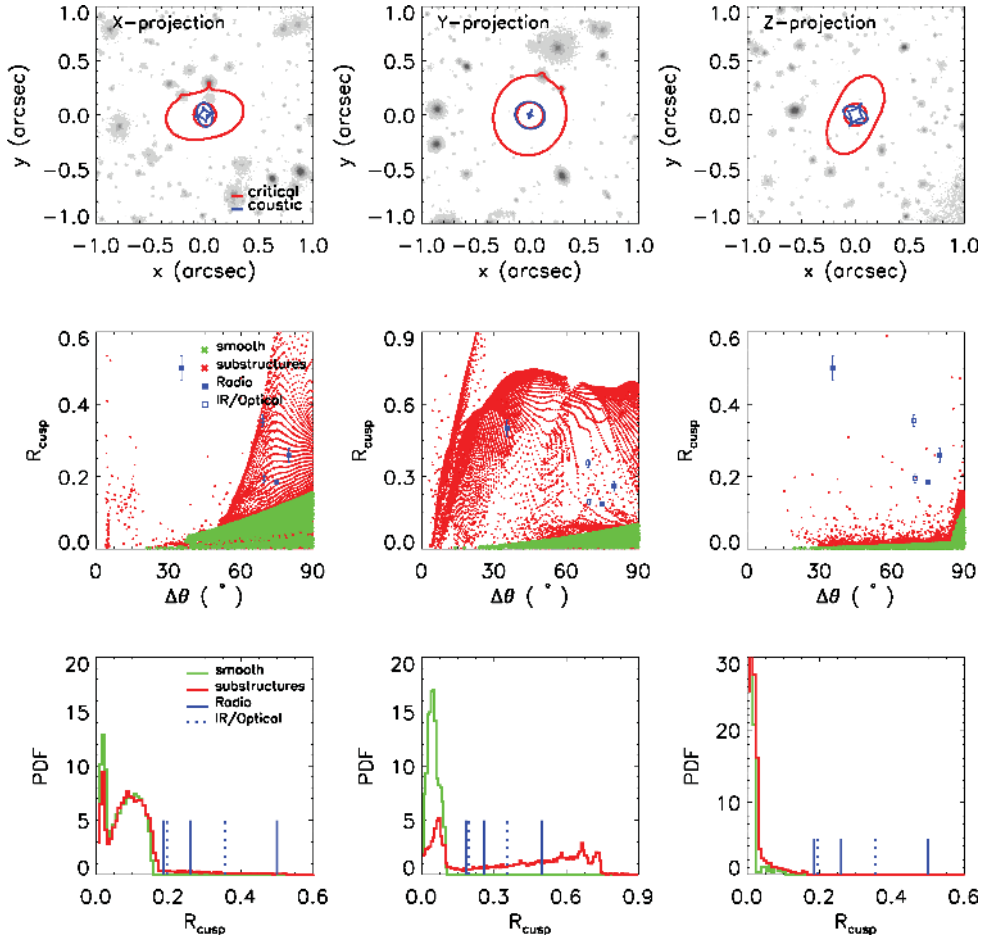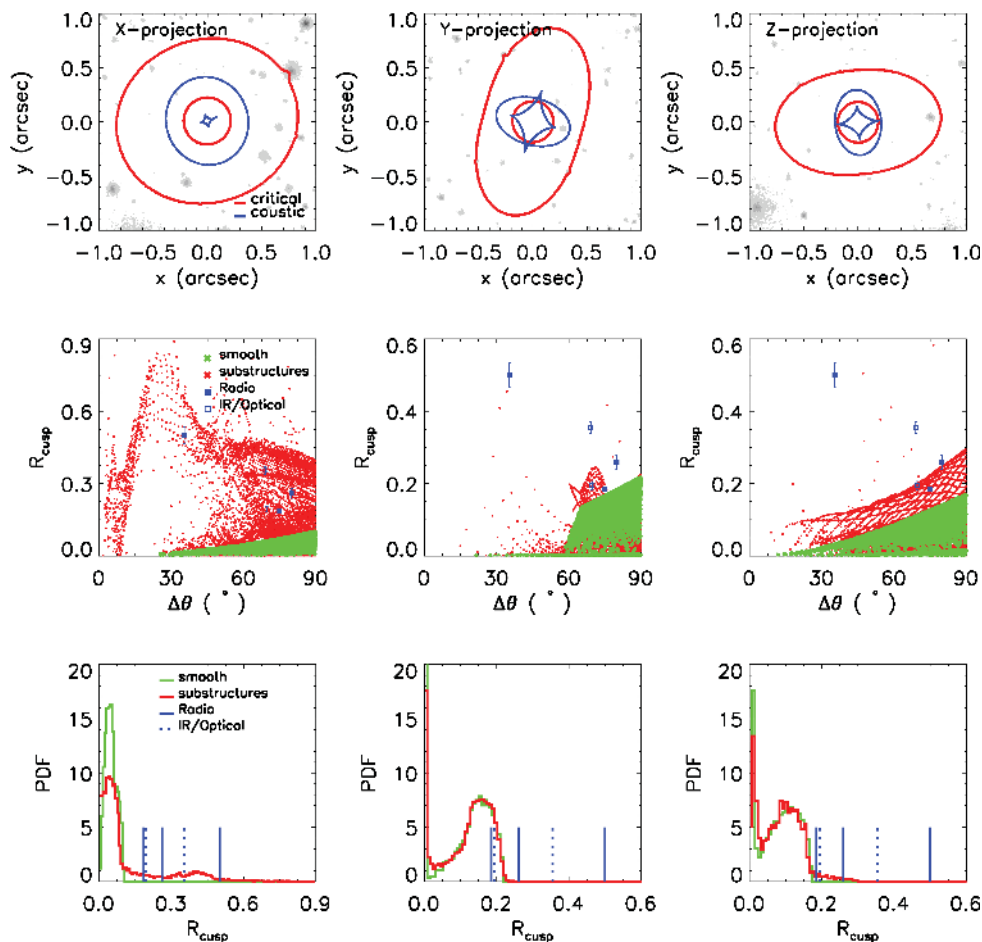
Figure 8. For the halo *Aq-B-2*, the symbols are the same as in Fig. 7. The truncated triangle pattern in the *Z*-projection is due to naked cusps of the central caustic. The strong violation of the cusp–caustic relation seen in the *Y*-projection is caused by subhaloes with $m_{sub} \leq 10^8 \, h^{-1} \, M_\odot$ with a violation rate $P(R_{cusp} \geq 0.187) = 64$ per cent.

profile), and study the violation of the cusp–caustic relation due to the dark matter substructures therein. In principle, we should compare the lensing properties of the simulated haloes with and without substructures in order to assess the effects of substructure. However, Fig. 6 shows a substantial broadening of the R_{cusp} distribution due to numerical noise, which will significantly confuse signals from real substructures.

As mentioned above, the total (dark matter plus baryons) mass profile of each halo is adjusted to resemble an isothermal distribution in the central region. To avoid excessive discreteness noise, we go one step further and adopt a fitted IE (with a density distribution given by equation 11) rather than the original particle distribution for subsequent lensing calculations. The parameters of the IE model are adjusted to match the original critical curves and the caustics of each Aquarius halo (together with the central galaxy) in a particular projection. We add the particle distributions of substructure in the Aquarius simulations (assigned to meshes according to the CIC algorithm) to the IE that fitted to the main galaxy halo, and compare its lensing properties with those of the smooth underlying IE. In this approach, the analytical solutions of the fitted isothermal ellipsoidal potential and its derivatives are tabulated on the image grid, including the cusp–caustic relation. By doing so, no Poisson noise of the underlying main halo is introduced, and so any confusion to the results from substructures is avoided.

We fit an isothermal ellipsoidal model to each of the three independent projections of each galaxy halo. The six fitting parameters are: (i) the effective critical radius b_I, (ii) the axis-ratio of the surface density ellipse q_3, (iii) the core radius S_0, (iv) and (v) the *X*- and *Y*-offsets of the projected centre X_c, Y_c and (vi) the rotation angle of the major axis of the surface density ellipse *RA*. The uncertainties of the fitted parameters are $\Delta b_I = 0.003$ arcsec, $\Delta q_3 = 0.01$, $\Delta S_0 = 0.001$ arcsec, $\Delta X_c = \Delta Y_c = 0.002$ arcsec and $\Delta RA = 0.004\pi$. The relative errors in the fitted critical curves and caustics are $\lesssim 10$ per cent for different projections of all the simulated galaxy haloes.

In Table 3, we list the IE parameters of the main haloes (b_I, q_3 and S_0). The critical radius b_I is of the order of 0.3 to 0.9 arcsec. The separation between images ($\sim 2b_I$) is in the range of the observed gravitational lenses (which peaks around 1 arcsec, see e.g. Browne et al. 2003). The axial ratios also match the observed lenses quite well. There is one exception, however. The core radius S_0 is quite large, of the order of 0.05–0.1 arcsec (corresponding to a few hundreds of pc). Such a core size is larger than those inferred from gravitational lenses which are in general consistent with zero core radius (e.g. Wallington & Narayan 1993; Oguri, Taruya & Suto 2001; Rusin & Ma 2001; Li & Ostriker 2003). This is a direct result of the implementation of the Hernquist profiles, which follow a logarithmic density slope of -1 in the central regions
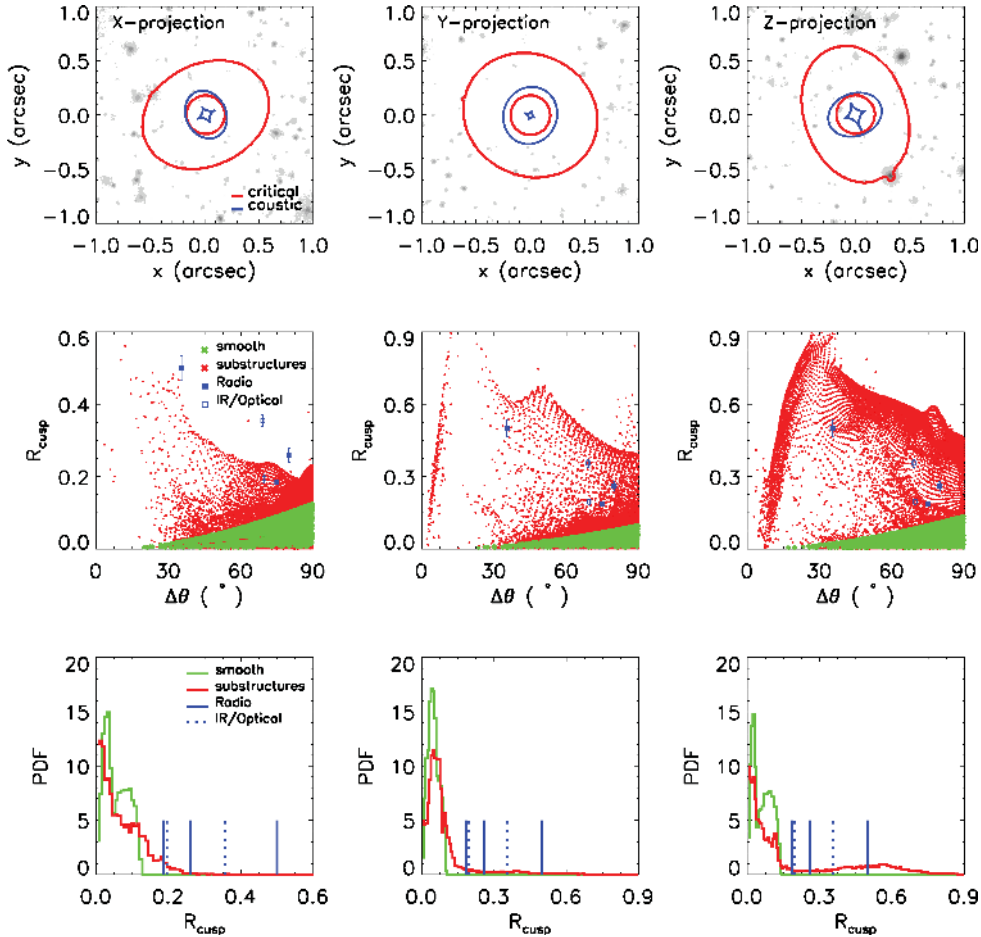
Figure 9. For the halo *Aq-C-2*, the symbols are the same as in Fig. 7. The truncated triangle pattern in the *Y*-projection is due to naked cusps of the central caustic. The halo in this projection has large ellipticity, which results in large $R_{\rm cusp}$ values. The strong violation in the *X*-projection is caused by subhaloes with $m_{\rm sub} \leq 10^8 \, h^{-1} \, {\rm M}_\odot$ with a violation rate $P(R_{\rm cusp} \geq 0.187) = 19$ per cent.

(see Fig. 1). However, this artefact should have little effects on the images we are interested in, which are close to the outer critical curve.

To examine the violation of the cusp–caustic relation, we generate about 10 000 cusp sources in each case, and calculate the resulting $R_{\rm cusp}$ distributions. All these cusp sources are inside the central caustic and close to the cusps, where the corresponding triple images have opening angles $\Delta\theta \leq 90°$. The results of all seven studied Aquarius haloes (in 21 projections) are given in Figs 7–13. As mentioned above, the probability density distribution of $R_{\rm cusp}$ often shows two peaks for the smooth haloes which are produced by the major and minor cusps, respectively. For the 'naked' cusp cases (where the central diamond caustic protrudes the outer elliptical caustic), the distributions of $R_{\rm cusp}$ versus the opening angle $\Delta\theta$ are somewhat truncated below certain opening angles (see Fig. 9 for the halo *Aq-C-2*'s *Y*-projection for an example). Empirically, it is rare for massive lensing galaxies to produce naked cusps. There is only one candidate APM08279 (Lewis et al. 2002), and that is likely due to lensing by an edge-on spiral rather than an elliptical. The four naked cusp cases from our simulations are caused by the large cores in the central density profiles of the lensing galaxies. We exclude these four naked cusp cases in the final statistic calculations (their inclusion does not significantly alter our results). Strong violations of the cusp–caustic relation due to substructures are seen in some

cases, e.g. for the *Y*-projection of the *Aq-B-2* halo (see Fig. 8). However, most of these cases have small cusp-lensing cross-sections (listed in Table 3, Column 8), defined as the areas covered by cusp sources whose images satisfy $\Delta\theta \leq 90°$. The mean probability of cusp violations calculated below are weighted by the cross-sections (see equation 12). As can be seen from Figs 7 to 12, the scatter in the cusp violation is large between different projections of different haloes. Also note that the halo *Aq-A-2* at $z = 0.6$ (Fig. 13) does not show a significant difference from the redshift-zero haloes in the violation of the cusp–caustic relation.

To see which massive substructures cause the cusp–caustic violation, we calculate the $R_{\rm cusp}$ distribution due to subhaloes more massive than 10^5, 10^6, 10^7 and $10^8 \, h^{-1} \, {\rm M}_\odot$, respectively. Fig. 14 shows one typical example, for the halo *Aq-D-2* along the *Z*-projection. We find that in most cases substructures with masses $m_{\rm sub} \leq 10^7$ to $10^8 \, h^{-1} \, {\rm M}_\odot$ dominate the contribution to the violations of the cusp–caustic relation (see the Column 9: $M_{\rm sub,cr}$ in Table 3). Note that previous studies on cusp violations typically resolve haloes larger than $\sim 10^8 \, h^{-1} \, {\rm M}_\odot$, and thus would not have been able to evaluate the effects of substructure accurately. However, the addition of subhaloes with $m_{\rm sub} \lesssim 10^6 \, h^{-1} \, {\rm M}_\odot$ does not appear to increase the violation frequency significantly (compare the three right panels). We return to the convergence issue as a function of subhalo mass in Section 5.

Figure 10. For the halo *Aq-D-2*, the symbols are the same as in Fig. 7. The strong violations in the *Y*- and *Z*-projection are caused by subhaloes with $m_{sub} \leq 10^7$ and $\leq 10^8 \, h^{-1} \, M_\odot$, respectively, with violation rates $P(R_{cusp} \geq 0.187) = 9.7$ per cent (*Y*-projection) and 31 per cent (*Z*-projection).

Note that most subhaloes that are projected close to the critical curves are due to chance alignment. Fig. 15 shows the spherical halocentric distance distribution for the subhaloes that are within a projected distance of $0.05 \, r_{200} \, (\sim 2.5$ Einstein radii). The fractions of subhaloes that are physically located within a spherical radius of $0.05 \, r_{200}$ are 15, 18, 15 and 0 per cent for subhaloes more massive than $10^5, 10^6, 10^7$ and $10^8 \, h^{-1} \, M_\odot$, respectively. The large median halocentric distances, $\sim 0.2 \, r_{200}$ in all cases, also show that projection effects are substantial.

4.2 Comparison with observations

Keeton et al. (2003) summarized 19 published quadruply imaged systems. Seven of them are detected at radio wavelengths.[4] Radio lenses are free from dust extinction. Due to their large emission regions, they are less likely to be affected by microlensing. In contrast, microlensing is likely to affect optical/IR flux ratios and so we treat them differently below.

[4] B0128+437 (Phillips et al. 2000), B0712+472 (Jackson et al. 1998; Jackson, Xanthopoulos & Browne 2000), B1422+231 (Impey et al. 1996; Patnaik & Narasimha 2001), B1555+375 (Marlow et al. 1999), B1608+656 (Koopmans & Fassnacht 1999), B1933+503 (Cohn et al. 2001) and B2045+265 (Fassnacht et al. 1999).

Dalal & Kochanek (2002) studied seven four-image radio-lensing systems: MG0414+0534 (Hewitt et al. 1992), B0712+472 (Jackson et al. 1998), PG1115+080 (Weymann et al. 1980), B1422+231 (Patnaik & Narasimha 2001), B1608+656 (Fassnacht et al. 1996), B1933+503 (Sykes et al. 1998) and B2045+265 (Fassnacht et al. 1999) and found that six show anomalous flux ratios, which might be due to the effects of substructure lensing. Among all the detected radio lenses, three (B0712+472, B1422+231 and B2045+265) show a typical cusp–caustic geometry (with $\Delta\theta \leq 90°$) and violations of the cusp–caustic relation. Another two lensing systems observed in the optical/IR band are also cusp–caustic lenses with $\Delta\theta \leq 90°$: RXJ1131−1231 (Sluse et al. 2003) and RXJ0911+0551 (Bade et al. 1997; Burud et al. 1998). Both have unexpected large values of R_{cusp}, which were shown to have been affected by microlensing (Morgan et al. 2006; Anguita et al. 2008). Table 2 lists the R_{cusp} and $\Delta\theta$ values for the five observed cusp–caustic lenses. Three out of the five cusp lenses are detected at radio wavelengths, thus their large R_{cusp} values are unlikely due to microlensing. We treat these three radio lenses as cusp–caustic violations due to substructure lensing. Below we will calculate the probability for the simulations to reproduce such an observed violation rate.

For each galaxy and each projection, we calculate the violation probability that the predicted R_{cusp} is larger than the observed R_{cusp}
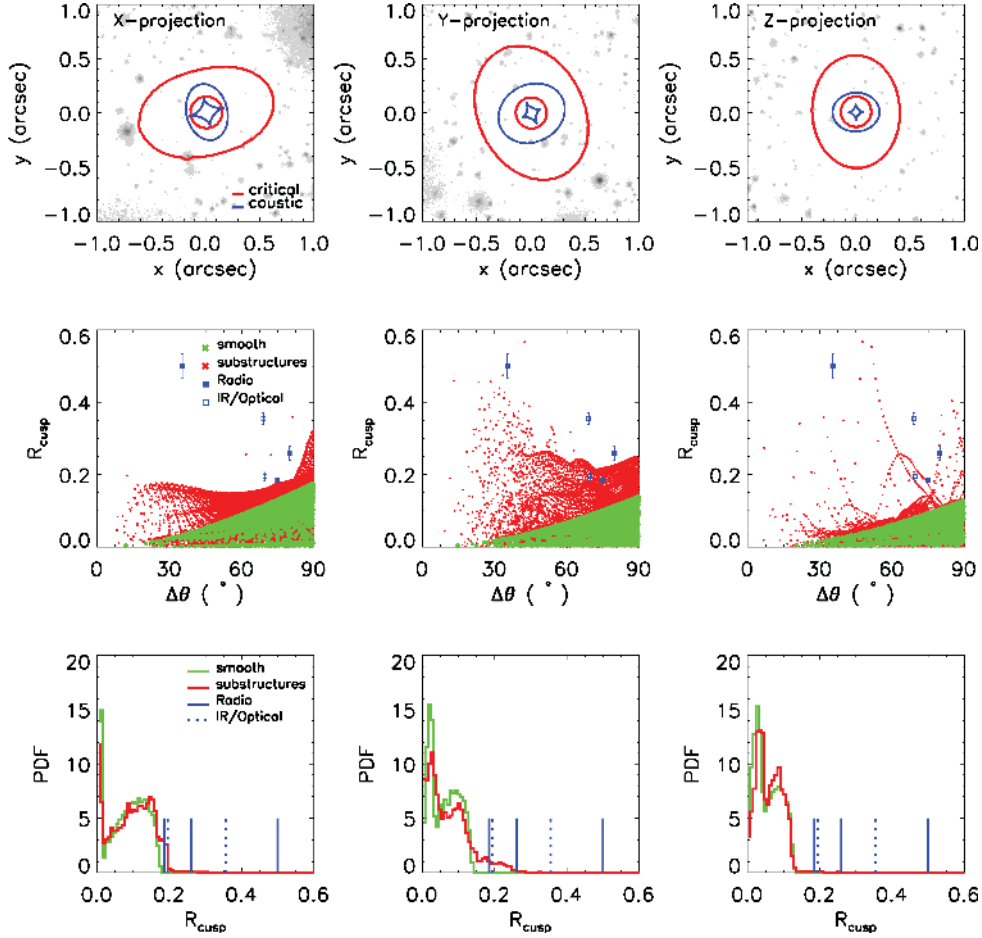
Figure 11. For the halo *Aq-E-2*, the symbols are the same as in Fig. 7.

value 0.187 for B1422+231, which shows the smallest violation (smallest R_{cusp} value) among the five cusp lenses. The cross-section weighted violation probability is given by

$$p_\sigma = \sum_i f_{\sigma,i} \, p_i(R_{\text{cusp}} \geq 0.187 | \Delta\theta \leq 90°), \quad f_{\sigma,i} = \frac{\sigma_i}{\sum_i \sigma_i}, \quad (12)$$

where the summation $i = 1, \ldots, (21 - 4)$ is for the seven haloes along the three independent projections of each, excluding the four naked cusp cases, and σ_i is the cross-section in the source plane for producing three close images with opening angle $\Delta\theta \leq 90°$. Using the above formula, we find the mean probability $p_\sigma \approx 0.064$ for $R_{\text{cusp}} \geq 0.187$. Note that this probability estimate is only approximate, since we have not considered the magnification bias (e.g. Turner et al. 1984).

To have three (radio) lensing cases with $R_{\text{cusp}} \geq 0.187$ (due to substructure lensing rather than microlensing) out of the five cusp lenses ($\Delta\theta \leq 90°$) observed so far, the probability is $C_5^3 p_\sigma^3 (1 - p_\sigma)^2 \approx 2.3 \times 10^{-3}$. The low probability suggests that the subhalo populations in the inner regions of the Aquarius haloes with Hernquist galaxies are insufficient to explain the observed frequency of flux anomalies in the cusp lenses.

5 DISCUSSION AND CONCLUSIONS

In this paper, we have used the ultra-high resolution Aquarius simulations to study the effects of substructure lensing. We incorporate the effects of baryons in the main halo by adding a stellar component (modelled as a Hernquist profile), and then take into account its effects on the dark matter halo through adiabatic contraction. The density profiles and lensing properties except the flux ratios are broadly consistent with the observed gravitational lenses. Using Monte Carlo simulations, we find large numerical noise for an isothermal halo populated with 10^8 particles, which shows considerable scatter in the R_{cusp} distribution for cusp lenses. In the end, we therefore study the substructure lensing by modelling the smooth underlying galaxy halo as an IE and superimposing the subhalo population from the Aquarius simulations. In this way, we focus on the lensing effects of subhaloes and avoid any confusion from numerical noise in the *N*-body realization of the simulated main haloes.

Our study finds that even with the much better resolved subhalo population of the Aquarius simulations, the observed cusp lenses still violate the cusp–caustic relation more frequently than predicted by *N*-body simulations.

The Aquarius haloes are Milky Way-type haloes in terms of their masses, while many lenses are ellipticals, which are more massive. Among the five cusp lenses we compare our results with, three of them (B2045+265, RXJ1131−1231, RXJ0911) are more
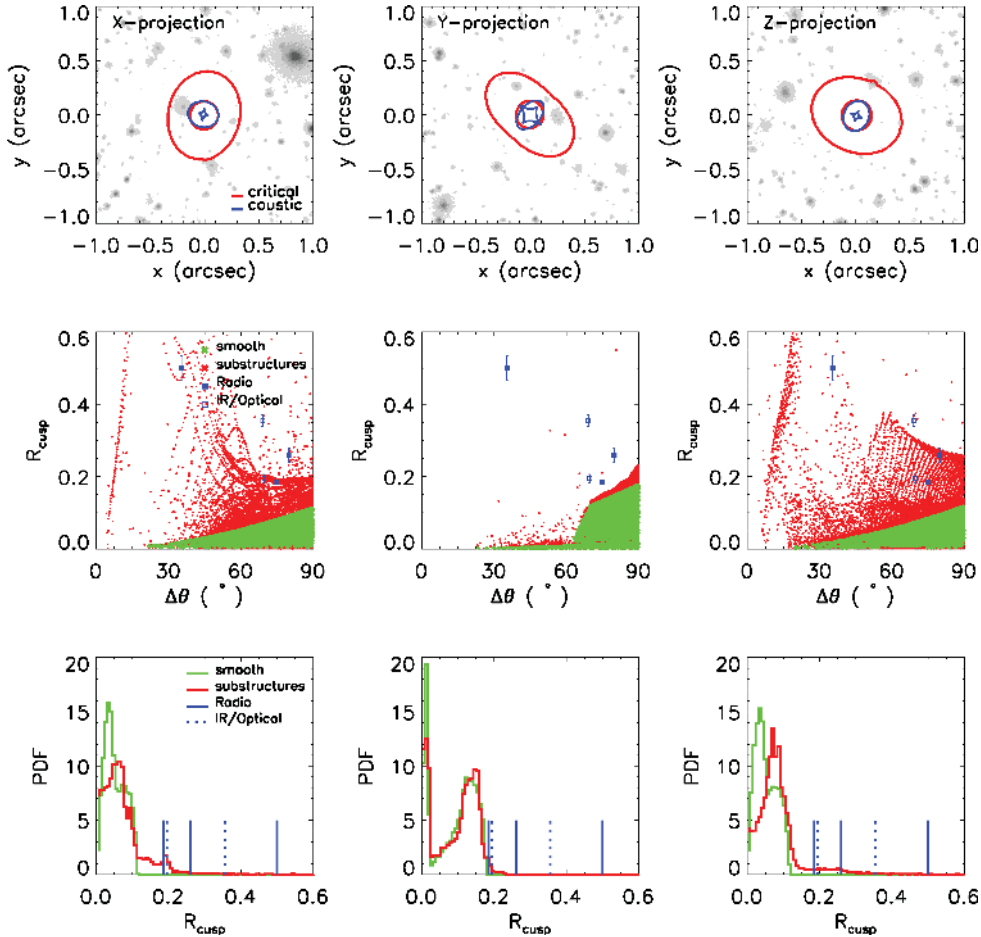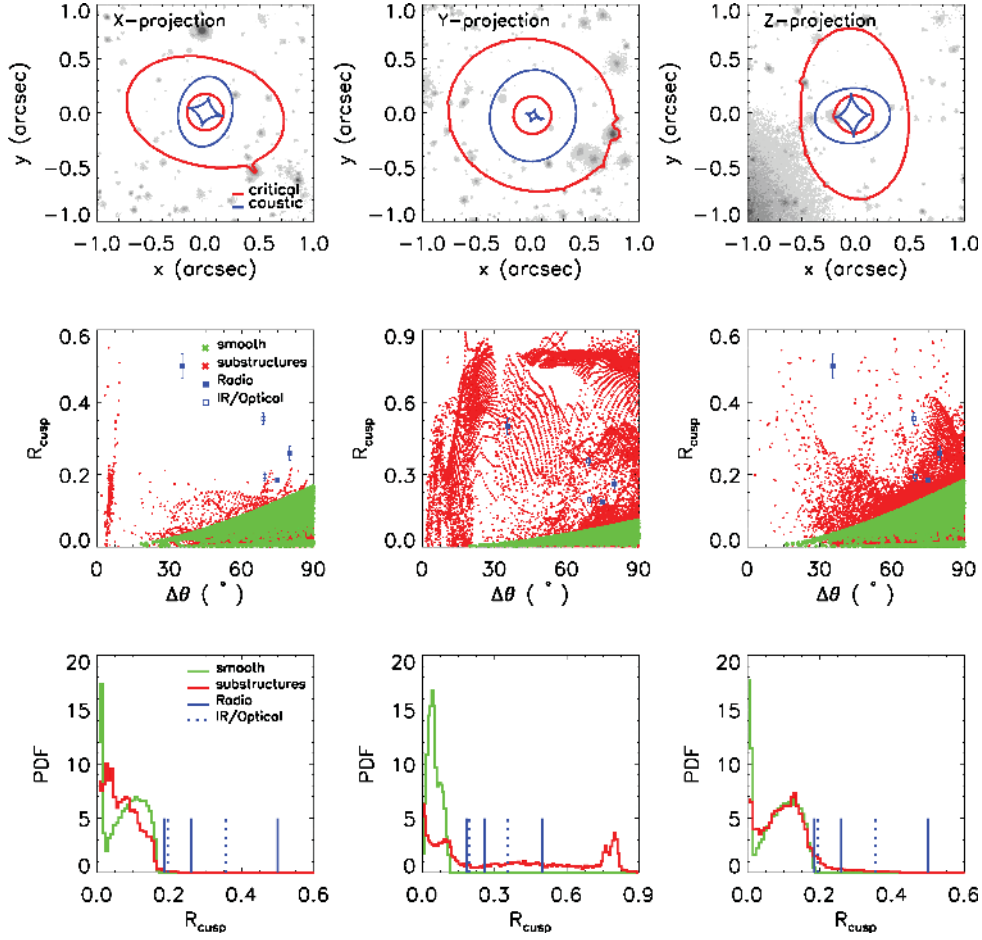
Figure 12. For the halo *Aq-F-2*, the symbols are the same as in Fig. 7. The truncated triangle pattern in the *Y*-projection is due to naked cusps of the central caustic. The strong violation in the *Z*-projection is mainly caused by subhaloes with $m_{sub} \leq 10^7 \, h^{-1} \, M_\odot$ with a violation rate $P(R_{cusp} \geq 0.187) = 6.7$ per cent.

massive than our simulated haloes and have Einstein radii twice as large as those of our haloes. The other two lenses (B0712+472, B1422+231) have Einstein radii and velocities (circular velocity or velocity dispersion) roughly comparable to the relatively massive haloes in the Aquarius simulations. As shown in Fig. 2 (the right-hand panel) the projected subhalo mass fraction increases with the projected radius *R*. If we have underestimated the Einstein radii b_I (e.g. because of uncertainties in the addition of the central galaxies), we could have potentially underestimated the violation rates due to the lack of enough substructures at smaller radii. We artificially increase the Einstein radii of the simulated haloes by a factor of 2 to study the violation probabilities due to a higher fraction of substructures at larger radii. The mean subhalo mass fraction within a 0.1 arcsec annulus around the new Einstein radius would increase from $f_{sub,annu} \approx 0.19$ to 0.24 per cent, and the mean violation probability would increase from $p_\sigma \approx 6.4$ to 14.0 per cent. The probability of reproducing the observed violation rate would increase from 0.2 to 2 per cent.

Another concern is that due to the finite particle mass in *N*-body simulations, the central cusps of the subhaloes may not be resolved, which may potentially result in an underestimation of the ability of the subhaloes to induce perturbations to the lensing potential. We consider an extreme case assuming all subhaloes are point-like sources with their masses and locations

from the simulations. In this scenario, $f_{sub,annu}$ roughly remains at 0.18 per cent, however, p_σ increases to 15.1 per cent. The probability to reproduce the observed violation rate increases to 2.5 per cent.

These low probabilities suggest that the subhalo populations in the central regions of the Aquarius haloes are not sufficient to explain the observed frequency of violations of the cusp–caustic relations. It is important to ask whether our results will change significantly if even lower mass subhaloes are resolved. We argue that this is unlikely to be the case. The total subhalo lensing cross-section is an integral of the cross-section of subhaloes of each mass weighted by their abundance. As shown in Section 4, most of the perturbing subhaloes have relatively low mass ($m_{sub} \leq 10^7$ to $10^8 \, h^{-1} \, M_\odot$). Their abundance scales as $dN(m_{sub})/dm_{sub} \propto m_{sub}^{-1.9}$. For a galaxy (subhalo) approximated by a SIS, the lensing cross-section roughly scales as σ^4 (e.g. Turner et al. 1984) where σ is the one-dimensional velocity dispersion. For Aquarius subhaloes, $m_{sub} \propto V_{max}^3$ (Springel et al. 2008), where V_{max} is the maximum circular velocity. If $\sigma \propto V_{max}$, then the integrated lensing cross-section will be $\propto m_{sub}^{0.43}$. On the other hand, for a point lens or an elliptical galaxy, the lensing cross-section is proportional to the lens mass, and the integrated lensing cross-section would be $\propto m_{sub}^{0.1}$. In all these cases, the subhalo lensing cross-sections are biased towards relatively massive subhaloes in the projected central region, and the incorporation

Figure 13. For the halo *Aq-A-2* at $z = 0.6$, the symbols are the same as in Fig. 7. The strong violation in the *Y*-projection is caused by subhaloes with $m_{sub} \leq 10^8 \, h^{-1} \, M_\odot$; a cusp violation rate is $P(R_{cusp} \geq 0.187) = 56$ per cent.
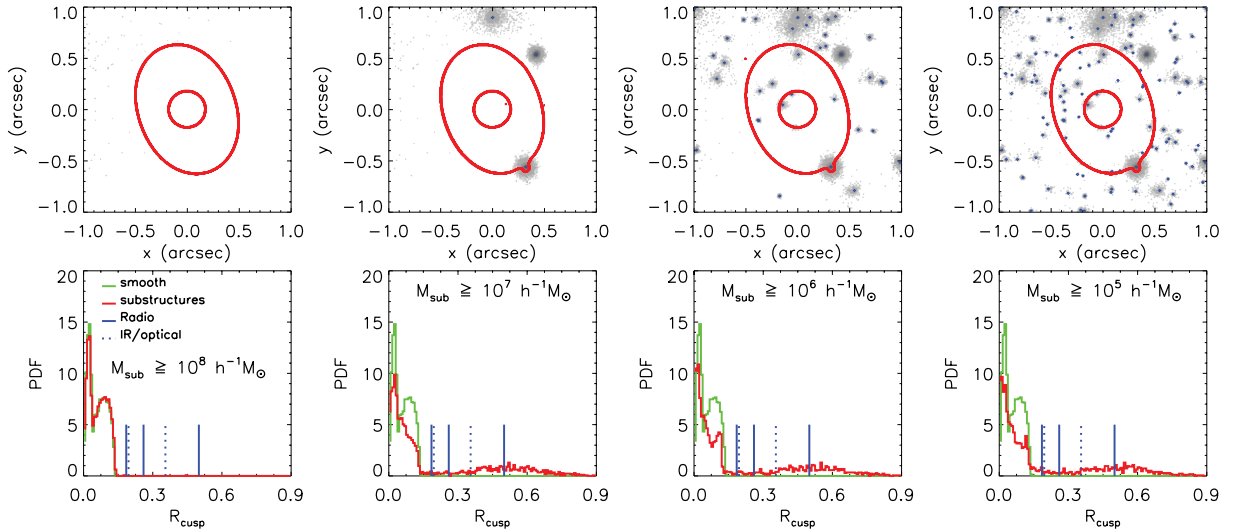
Figure 14. Effects of substructure lensing as a function of the lower cut-off subhalo mass for the halo *Aq-D-2* along the *Z*-projection. The upper panels show the projected substructures with masses above a threshold. The projected centres of the subhaloes and the corresponding critical curves are plotted at the top. From the left to the right, the lower cut-off subhalo mass changes from $10^8, 10^7, 10^6$ to $10^5 \, h^{-1} \, M_\odot$. The bottom panels show the corresponding probability distribution functions of R_{cusp}. Most substructures that survive and are projected within the central few kpc are low-mass subhaloes ($\leq 10^8 \, h^{-1} \, M_\odot$), which dominate the violation of the cusp–caustic relation.
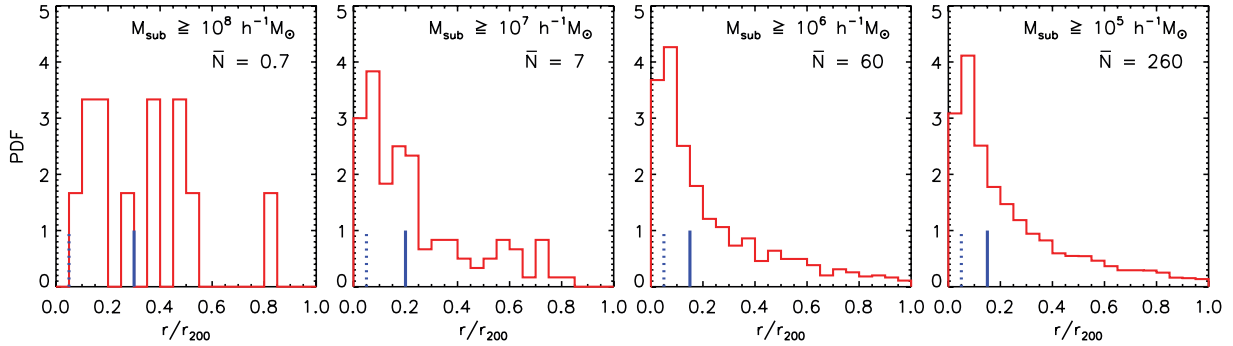
Figure 15. Distribution of halocentric distances of the subhaloes projected within 0.05 r_{200} (~ 2.5 times the Einstein radius, indicated by the dotted line in each panel). The solid lines give the median spherical halocentric distances of the subhaloes; all are around 0.2 r_{200}. The average number of subhaloes $\bar{N}$ is indicated inside each panel.

Table 2. The image opening angle and R_{cusp} for the observed cusp–caustic lenses, taken from Amara et al. (2006).

Lens	$\Delta\theta$	R_{cusp}	Band
B0712+472	79.8°	0.26 ± 0.02	Radio
B2045+265	35.3°	0.501 ± 0.035	Radio
B1422+231	74.9°	0.187 ± 0.006	Radio
RXJ1131 − 1231	69.0°	0.355 ± 0.015	Optical/IR
RXJ0911 + 0551	69.6°	0.192 ± 0.011	Optical/IR

of even lower mass subhaloes should not change our results significantly.

We mention in passing that a warm dark matter scenario would suppress the formation of small subhaloes, making it even more difficult to explain the observed cusp violations (see e.g. Miranda & Macciò 2007). Below, we compare our study with previous work, before discussing its limitations and outlining possible future work.

5.1 Comparison with previous studies

There have been a number of studies of substructure lensing using numerically simulated haloes, including those from hydrodynamical simulations. Below we compare a few of these studies with our own.

Dalal & Kochanek (2002) concluded that at the 90 per cent confidence level, a substructure fraction of 0.6 to 7 per cent can explain the observed anomalous flux ratio. For the Aquarius subhalo population, Table 3 Column 5: $f_{sub,annu}$ shows such fraction averaged over a thin annulus around the outer tangential curve, which is always below 1 per cent, sometimes much smaller (not to be confused with f_{sub} in Table 1 and Fig. 2, which refers to the subhalo mass fraction within r_{200}). This is the primary reason why our predicted cusp violations are smaller than the observed violation frequencies.

Bradač et al. (2004) used hydrodynamical simulations of Steinmetz & Navarro (2002) and concluded that the predicted cusp violations due to substructure are comparable to those observed. Their simulated halo has $\sim 10^5$ particles, resolving subhaloes down to $5 \times 10^8 \, M_\odot$. As the authors pointed out, the numerical noise may be as high as 5 per cent. The observed high-order singularities in their simulations are much higher than ours (comparable to the caustic structure shown in Fig. 5 for 10^6 particles). It is possible

that their high numerical noise may have produced too many artificial violations, although we note that they used Voroni density estimation to reduce the discreteness noise.

Our conclusion that the dark matter subhalo population may be insufficient to explain the observed cusp violations is consistent with Mao et al. (2004), Amara et al. (2006), Macciò et al. (2006) and Macciò & Miranda (2006). The number of particles used in those studies is roughly two orders of magnitude smaller than here. In particular, the study by Mao et al. (2004) found large scatter among different haloes, a conclusion confirmed by our results.

5.2 Limitations of the present study and future work

The most severe limitation of our study is that the high-resolution simulations used here include only dark matter. Without baryons, these haloes are subcritical (see Section 2) and incapable of producing multiple images. We are, therefore, forced to incorporate a model for the baryonic galaxy at the centre of each halo. The galaxy changes not only the overall dark matter profiles (taken into account by adiabatic contraction) but also the dynamical evolution of subhaloes, an effect which is not considered here. On the one hand, the increased baryonic density at the centre of the halo will make the subhaloes feel stronger tidal forces, particularly those that come close to the centre. On the other hand, the baryons within subhaloes will make them more resilient to tidal disruption. It is not clear which effect will dominate. We comment, however, that the subhaloes that come very close to the centre may have already been tidally stripped or disrupted, and thus most of the surviving subhaloes that can be identified by SUBFIND may have quite large pericentre passages. As a result, the effects of baryons in the host halo may not change the results very significantly. However, we caution that SUBFIND, like most substructure finders, has difficulties in identifying subhaloes in the densest regions of the halo and assigning them correct masses. Empirically the Milky Way does not seem to host many luminous satellites close to the centre. Hydrodynamical simulations can in principle address this issue directly (subject to the uncertainties in the treatment of gas processes). Macciò et al. (2006) found a factor of 2 increase in the number of surviving satellite galaxies (with masses above $10^7 \, M_\odot$) in the centres of galaxies when including baryons in the CDM simulations, but concluded that even this was not sufficient to explain the flux anomaly problem.

Observationally, it is interesting that more than one half of the CLASS lenses appear to show luminous companion galaxies in

Table 3. Substructure-lensing parameters of Aquarius haloes.

Halo name projection	b_I (arcsec)	q_3	S_0 (arcsec)	$f_{sub,annu}$ (per cent)	$\alpha_{sub,max}$ (arcsec)	$P(R_{cusp} \geq 0.187)$ (per cent)	$f_\sigma(\Delta\theta \leq 90°)$ (per cent)	$M_{sub,cr}$ ($h^{-1} M_\odot$)
Aq-A-2								
X-projection	0.602	0.77	0.103	0.11	0.065	5.90	4.85	10^7 ⇓
Y-projection	0.657	0.78	0.092	0.69	0.059	1.26	5.76	10^8 ⇑
Z-projection	0.647	0.76	0.091	0.01	0.055	0.08	6.59	10^7 ⇓
Aq-B-2								
X-projection	0.306	0.73	0.076	0.42	0.008	5.91	2.16	—
Y-projection	0.408	0.91	0.071	0.48	0.007	64.13	0.41	10^8 ⇓
Z-projection	0.286	0.64	0.080	0.09	0.012	0.09	0.77	—
Aq-C-2								
X-projection	0.846	0.91	0.085	0.13	0.015	19.09	1.07	10^8 ⇓
Y-projection	0.571	0.60	0.107	0.06	0.002	13.98	21.41	—
Z-projection	0.589	0.70	0.104	0.03	0.007	3.71	10.58	10^7 ⇓
Aq-D-2								
X-projection	0.576	0.83	0.101	0.13	0.006	3.79	2.13	10^7 ⇓
Y-projection	0.655	0.91	0.088	0.06	0.005	9.72	0.57	10^7 ⇓
Z-projection	0.583	0.79	0.101	0.40	0.011	30.58	4.48	10^8 ⇓
Aq-E-2								
X-projection	0.473	0.69	0.076	0.18	0.020	3.04	7.62	10^8 ⇓
Y-projection	0.548	0.79	0.056	0.13	0.007	5.40	3.29	10^7 ⇓
Z-projection	0.474	0.82	0.069	0.05	0.006	0.65	1.59	10^7 ⇓
Aq-F-2								
X-projection	0.416	0.86	0.080	0.19	0.021	5.83	0.67	10^8 ⇓
Y-projection	0.370	0.67	0.091	0.09	0.009	1.38	3.78	—
Z-projection	0.435	0.85	0.088	0.22	0.012	6.74	0.78	10^8 ⇓
Aq-A-2 ($z = 0.6$)								
X-projection	0.568	0.71	0.079	0.11	0.008	0.60	7.75	10^8 ⇓
Y-projection	0.731	0.89	0.054	0.70	0.022	55.81	1.74	10^8 ⇓
Z-projection	0.592	0.69	0.082	0.33	0.083	7.56	12.00	10^8 ⇓

Note. Columns 2–4: b_I, q_3 and S_0, the Einstein radius, axis ratio and core radius of the fitted IE (see equation 11); Column 5: $f_{sub,annu}$ is the subhalo mass fraction within a 0.1 arcsec annulus around the outer critical curve; Column 6: $\alpha_{sub,max}$ is the maximum magnitude in the projected central 2×2 arcsec^2 region of the deflection angle due to all substructures within r_{200}, usually found close to an individual subhalo; Column 7: $P(R_{cusp} \geq 0.187)$ is the probability (in per cent) for sources with $\Delta\theta \leq 90°$ (defined as 'cusp sources') to have $R_{cusp} \geq 0.187$, referred to as the 'cusp–caustic violation probability'; Column 8: $f_\sigma(\Delta\theta \leq 90°)$ is the cross-section weight (as defined in equation 12) in the source plane for producing three close images with opening angle $\Delta\theta \leq 90°$; Column 9: $M_{sub,cr}$ is the critical subhalo mass that causes the strong violation of the cusp–caustics relation. Arrows indicate 'above' or 'below'. Lenses with naked cusps of the caustics always have low cusp–caustic violations (although their large ellipticities may result in large R_{cusp} values) and are labelled as '—'.

projection (Bryan et al. 2008; Jackson, in preparation), and their inclusion in the models appears to alleviate the anomalous flux ratio problem (see below). This may be just a statistical fluke due to the small sample size (22 lenses in total) or some of these may be due to chance alignment along the line-of-sight (Chen et al. 2003; Wambsganss et al. 2005; Metcalf 2005a,b; Miranda & Macciò 2007). Nevertheless, for the three radio lenses that show apparent cusp violations (see Table 2), the most serious case is B2045+265 with $R_{cusp} \approx 0.5$. Recently, McKean et al. (2007) found a galaxy, G2, which is about 0.66 arcsec away from the main lensing galaxy G1 (at redshift 0.867), and about 3.6 to 4.5 mag fainter than G1 depending on the wavelength. The photometric redshift of G2 is consistent with that of G1 (although also consistent with a redshift ∼4–5). The inclusion of this faint satellite galaxy in the model can explain the flux anomaly reasonably well, although the satellite is required to be very flattened with an axis ratio of 8:1, which may not be realistic. This case highlights the potential roles that the luminous satellites may play in the anomalous flux ratio problem.

We note, however, that numerical simulations by Dolag et al. (2008) showed that star-dominated galaxies (not traced by dark matter only simulations) appear to contribute only ∼10 per cent of the subhalo population in clusters of galaxies. It is unclear, however, whether this cluster-based result can be extrapolated to galaxy scales where cooling is more efficient. We plan to use semi-analytical galaxy catalogues in the Aquarius simulations to address this issue more quantitatively in subsequent work.

Substructures not only perturb the flux ratios, but also affect the image positions. In Table 3, we show the maximum perturbation of the deflection angle, $\alpha_{sub,max}$, within the central 2×2 arcsec^2 region, produced by all the subhaloes within r_{200}. The maximum deviations range from a few milliarcseconds to <0.1 arcsec. They may leave observable signatures on close pair images such as that observed in MG2016+112 (Koopmans et al. 2002; More et al. 2009). We find that most of these astrometric deviations are dominated by one large, nearby subhalo. This clearly warrants further work in the near future.

ACKNOWLEDGMENTS

REFERENCES

Abadi M. G., Navarro J. F., Fardal M., Babul A., Steinmetz M., 2009, preprint (arXiv:0902.2477)

Amara A., Metcalf R. B., Cox T. J., Ostriker J. P., 2006, MNRAS, 367, 1367

Anguita T., Faure C., Yonehara A., Wambsganss J., Kneib J.-P., Covone G., Alloin D., 2008, A&A, 481, 615

Bade N., Siebert J., Lopez S., Voges W., Reimers D., 1997, A&A, 317, L13

Barnes J., White S. D. M., 1984, MNRAS, 211, 753

Belokurov V. et al., 2007, ApJ, 654, 897

Benson A. J., Frenk C. S., Lacey C. G., Baugh C. M., Cole S., 2002, MNRAS, 333, 177

Biggs A. D., Browne I. W. A., Jackson N. J., York T., Norbury M. A., McKean J. P., Phillips P. M., 2004, MNRAS, 350, 949

Blandford R., Narayan R., 1986, ApJ, 310, 568

Blumenthal G. R., Faber S. M., Flores R., Primack J. R., 1986, ApJ, 301, 27

Bolton A. S., Treu T., Koopmans L. V. E., Gavazzi R., Moustakas L. A., Burles S., Schlegel D. J., Wayth R., 2008, ApJ, 684, 248

Bradač M., Schneider P., Lombardi M., Steinmetz M., Koopmans L. V. E., Navarro J. F., 2004, A&A, 423, 797

Browne I. W. A. et al., 2003, MNRAS, 341, 13

Bryan S. E., Mao S., Kay S. T., 2008, MNRAS, 391, 959

Bullock J. S., Kravtsov A. V., Weinberg D. H., 2000, ApJ, 539, 517

Burud I. et al., 1998, ApJ, 501, L5

Chen J., Kravtsov A. V., Keeton C. R., 2003, ApJ, 592, 24

Chen J., Rozo E., Dalal N., Taylor J. E., 2007, ApJ, 659, 52

Chiba M., 2002, ApJ, 565, 17

Chiba M., Minezaki T., Kashikawa N., Kataza H., Inoue K. T., 2005, ApJ, 627, 53

Cohn J. D., Kochanek C. S., McLeod B. A., Keeton C. R., 2001, ApJ, 554, 1216

Congdon A. B., Keeton C. R., 2005, MNRAS, 364, 1459

Congdon A. B., Keeton C. R., Nordgren C. E., 2008, MNRAS, 389, 398

Dalal N., Kochanek C. S., 2002, ApJ, 572, 25

Diemand J., Kuhlen M., Madau P., 2007, ApJ, 657, 262

Dolag K., Borgani S., Murante G., Springel V., 2008, preprint (arXiv:0808.3401)

Efstathiou G., 1992, MNRAS, 256, 43P

Einasto J., 1965, Trudy Inst. Astroz. Alma-Ata, 51, 87

Evans N. W., Witt H. J., 2003, MNRAS, 345, 1351

Fassnacht C. D., Womble D. S., Neugebauer G., Browne I. W. A., Readhead A. C. S., Matthews K., Pearson T. J., 1996, ApJ, 460, L103

Fassnacht C. D. et al., 1999, AJ, 117, 658

Gao L., De Lucia G., White S. D. M., Jenkins A., 2004a, MNRAS, 352, L1

Gao L., White S. D. M., Jenkins A., Stoehr F., Springel V., 2004b, MNRAS, 355, 819

Gavazzi R., Treu T., Rhodes J. D., Koopmans L. V. E., Bolton A. S., Burles S., Massey R. J., Moustakas L. A., 2007, ApJ, 667, 176

Ghigna S., Moore B., Governato F., Lake G., Quinn T., Stadel J., 2000, ApJ, 544, 616

Gnedin N. Y., 2000, ApJ, 542, 535

Gnedin O. Y., Kravtsov A. V., Klypin A. A., Nagai D., 2004, ApJ, 616, 16

Hernquist L., 1990, ApJ, 356, 359

Hewitt J. N., Turner E. L., Lawrence C. R., Schneider D. P., Brody J. P., 1992, AJ, 104, 968

Hockney R. W., Eastwood J. W., 1981, Computer Simulation Using Particles. Computer Simulation Using Particles, McGraw-Hill, New York

Impey C. D., Foltz C. B., Petry C. E., Browne I. W. A., Patnaik A. R., 1996, ApJ, 462, L53

Jackson N. et al., 1998, MNRAS, 296, 483

Jackson N., Xanthopoulos E., Browne I. W. A., 2000, MNRAS, 311, 389

Jiang G., Kochanek C. S., 2007, ApJ, 671, 1568

Kauffmann G., White S. D. M., Guiderdoni B., 1993, MNRAS, 264, 201

Keeton C. R., 2001, ApJ, 561, 46

Keeton C. R., Kochanek C. S., 1998, ApJ, 495, 157

Keeton C. R., Moustakas L. A., 2009, ApJ, 699, 1720

Keeton C. R., Gaudi B. S., Petters A. O., 2003, ApJ, 598, 138

Klypin A., Kravtsov A. V., Valenzuela O., Prada F., 1999, ApJ, 522, 82

Kochanek C. S., 1991, ApJ, 373, 354

Kochanek C. S., Dalal N., 2004, ApJ, 610, 69

Kochanek C. S., White M., 2001, ApJ, 559, 531

Koopmans L. V. E., Fassnacht C. D., 1999, ApJ, 527, 513

Koopmans L. V. E., Garrett M. A., Blandford R. D., Lawrence C. R., Patnaik A. R., Porcas R. W., 2002, MNRAS, 334, 39

Koopmans L. V. E. et al., 2003, ApJ, 595, 712

Koopmans L. V. E., Treu T., Bolton A. S., Burles S., Moustakas L. A., 2006, ApJ, 649, 599

Lewis G. F., Carilli C., Papadopoulos P., Ivison R. J., 2002, MNRAS, 330, L15

Li L.-X., Ostriker J. P., 2003, ApJ, 595, 603

Li G.-L., Mao S., Jing Y. P., Kang X., Bartelmann M., 2006, ApJ, 652, 43

Macciò A. V., Miranda M., 2006, MNRAS, 368, 599

Macciò A. V., Moore B., Stadel J., Diemand J., 2006, MNRAS, 366, 1529

Madau P., Diemand J., Kuhlen M., 2008, ApJ, 679, 1260

Mao S., 1992, ApJ, 389, 63

Mao S., Schneider P., 1998, MNRAS, 295, 587

Mao S., Jing Y., Ostriker J. P., Weller J., 2004, ApJ, 604, L5

Marlow D. R. et al., 1999, AJ, 118, 654

McKean J. P. et al., 2007, MNRAS, 378, 109

Metcalf R. B., 2002, ApJ, 580, 696

Metcalf R. B., 2005a, ApJ, 622, 72

Metcalf R. B., 2005b, ApJ, 629, 673

Metcalf R. B., Madau P., 2001, ApJ, 563, 9

Metcalf R. B., Zhao H., 2002, ApJ, 567, L5

Metcalf R. B., Moustakas L. A., Bunker A. J., Parry I. R., 2004, ApJ, 607, 43

Miranda M., Macciò A. V., 2007, MNRAS, 382, 1225

Mo H. J., Mao S., White S. D. M., 1998, MNRAS, 295, 319

Monaghan J. J., 1992, ARA&A, 30, 543

Moore B., Ghigna S., Governato F., Lake G., Quinn T., Stadel J., Tozzi P., 1999, ApJ, 524, L19

More A., McKean J. P., More S., Porcas R. W., Koopmans L. V. E., Garrett M. A., 2009, MNRAS, 394, 174

Morgan N. D., Kochanek C. S., Falco E. E., Dai X., 2006, BAAS, 38, 927

Myers S. T. et al., 2003, MNRAS, 341, 1

Natarajan P., De Lucia G., Springel V., 2007, MNRAS, 376, 180

Navarro J. F., Frenk C. S., White S. D. M., 1996, ApJ, 462, 563

Navarro J. F., Frenk C. S., White S. D. M., 1997, ApJ, 490, 493

Navarro J. F. et al., 2008, preprint (arXiv:0810.1522)

Oguri M., 2002, ApJ, 580, 2

Oguri M., Taruya A., Suto Y., 2001, ApJ, 559, 572

Patnaik A. R., Narasimha D., 2001, MNRAS, 326, 1403

Phillips P. M. et al., 2000, MNRAS, 319, L7
Rusin D., Kochanek C. S., 2005, ApJ, 623, 666
Rusin D., Kochanek C. S., Keeton C. R., 2003, ApJ, 595, 29
Rusin D., Ma C.-P., 2001, ApJ, 549, L33
Schechter P. L., Wambsganss J., 2002, ApJ, 580, 685
Schneider P., Weiss A., 1992, A&A, 260, 1
Schneider P., Ehlers J., Falco E. E., 1992, Gravitational Lenses, Vol. XIV. Springer-Verlag, Berlin, p. 560
Schneider P., Kochanek C. S., Wambsganss J., 2006, Gravitational Lensing: Strong, Weak and Micro. Saas-Fee Advanced Courses, Vol. 33. Springer-Verlag, Berlin
Sluse D. et al., 2003, A&A, 406, L43
Spergel D. N. et al., 2007, ApJS, 170, 377
Springel V., 2005, MNRAS, 364, 1105
Springel V., Yoshida N., White S. D. M., 2001, New Astron., 6, 79
Springel V. et al., 2008, MNRAS, 391, 1685
Steinmetz M., Navarro J. F., 2002, New Astron., 7, 155

Sugai H., Kawai A., Shimono A., Hattori T., Kosugi G., Kashikawa N., Inoue K. T., Chiba M., 2007, ApJ, 660, 1016
Sykes C. M. et al., 1998, MNRAS, 301, 310
Thoul A. A., Weinberg D. H., 1996, ApJ, 465, 608
Treu T., Koopmans L. V. E., 2004, ApJ, 611, 739
Turner E. L., Ostriker J. P., Gott J. R. III, 1984, ApJ, 284, 1
Wallington S., Narayan R., 1993, ApJ, 403, 517
Wambsganss J., Bode P., Ostriker J. P., 2005, ApJ, 635, L1
Weymann R. J. et al., 1980, Nat, 285, 641
Williams L. L. R., Navarro J. F., Bartelmann M., 1999, ApJ, 527, 535
Yoo J., Kochanek C. S., Falco E. E., McLeod B. A., 2005, ApJ, 626, 51
Yoo J., Kochanek C. S., Falco E. E., McLeod B. A., 2006, ApJ, 642, 22
Zhang M., 2008, PhD thesis, University of Manchester

This paper has been typeset from a TEX/LATEX file prepared by the author.